Multi-Scale Pixel and Slope-Unit Landslide Susceptibility Mapping with Applicability-Domain Validation: Evidence from the Karnali Highway Corridor, Western Nepal

Ayush Karki[a], Aakash Mandal[a], Amrit Bhusal[a], Akhilesh Kumar Karna[a]

[a]*Department of Civil Engineering- Pulchowk Campus, Tribhuvan University, Nepal*

This is a non-peer-reviewed preprint submitted to EarthArXiv. This manuscript has been submitted to Georisk: Assessment and Management of Risk for Engineered Systems and Geohazards (Taylor & Francis) and is currently under review.

Multi-Scale Pixel and Slope-Unit Landslide Susceptibility Mapping with Applicability-Domain Validation: Evidence from the Karnali Highway Corridor, Western Nepal

Ayush Karki[a], Aakash Mandal[a], Amrit Bhusal[a], Akhilesh Kumar Karna[a]

[a]*Department of Civil Engineering- Pulchowk Campus, Tribhuvan University, Nepal*

ABSTRACT

Landslides along Himalayan Road corridors cause repeated loss of life and prolonged disruption of access, yet susceptibility products for these settings rarely report how far their predictions can be trusted away from the training data. This study maps landslide susceptibility for the Karnali Highway (NH 58) corridor in western Nepal (about 2,155 km^2) and pairs the map with an explicit reliability layer. A landslide inventory and an equal set of non-landslide sites were characterised by nine conditioning factors spanning topography, hydrology, geology, land cover, and proximity to roads and drainage. Two mapping units were compared: a pixel representation evaluated at three moving-window sizes (3x3, 15x15, 25x25 cells on a 12.5 m DEM) and a slope-unit representation. Random Forest, a radial-basis support vector machine, and XGBoost were tuned with Bayesian search, calibrated with Platt scaling, and combined as an equal-weight mean-probability ensemble. To avoid the optimistic scores that spatial autocorrelation produces under random splitting, all tuning and evaluation used spatially blocked cross-validation with 1,000 m centroid blocks for the pixel pipeline and stratified random cross-validation for the slope-unit pipeline. Under this blocking the pixel models reached a mean cross-validation AUC of 0.96 to 0.98 across models and scales, with XGBoost the strongest; the single blocked-holdout fold reached 0.99 at the 15x15 window and is reported as a secondary diagnostic. The slope-unit models, a more conservative mapping unit, scored 0.76 to 0.91. Performance peaked at the intermediate window and declined at 25x25. Aspect was the leading predictor across every model and scale, followed by NDVI, slope, and the topographic wetness index, a pattern that points to monsoon-driven moisture loading on south-to-southwest-facing slopes. About 37 percent of the corridor falls in the combined High and Very High pixel susceptibility classes. A Mahalanobis-distance applicability domain, blended with inter-model agreement and published as a binary trusted/untrusted mask, flags where the prediction extrapolates beyond the training feature space; about 98 percent of slope units, and a comparable share of pixels, fell inside the trusted domain, giving practitioners a spatial guide to where the map should and should not drive engineering decisions

Keywords: landslide susceptibility; machine learning ensemble; XGBoost; slope units; applicability domain; Nepal Himalaya

1 INTRODUCTION

Landslides are among the most widespread and lethal natural hazards, occurring on every continent except Antarctica and causing recurring loss of life, livelihoods, and infrastructure (Froude & Petley, 2018a). Global catalogues consistently show occurrence and fatalities concentrating in Asia, and specifically along the Himalayan arc Kirschbaum et al., 2015), (Petley, 2012), (Froude & Petley, 2018b),, Gómez et al., 2023).

Nepal ranks among the countries with the highest per-capita landslide fatality risk (Kincey et al., 2024a), (Nadim et al., 2006), owing to steep topography, an intense monsoon, and active tectonics along the Himalayan front (Harvey et al., 2025a). Occurrence is episodic and spatially erratic within a monsoon season, and the frequency–fatality relationship is strongly non-linear, so a few high-magnitude, poorly anticipated events dominate the human toll (Adhikari & Tian, 2021).

Two events illustrate this. The August 2014 Jure landslide in Sindhupalchok District killed about 156 people, dammed the Sunkoshi River for weeks, and severed the Arniko Highway; the poorest affected households lost up to fourteen times their annual income (van der Geest, 2018). The April 2015 Mw 7.8 Gorkha earthquake triggered more than 20,000 landslides across 14 districts, and the elevated hazard persisted for years, with the 2020 monsoon alone producing dozens of fatal landslides in the affected zone (Harvey et al., 2025b).

Landslides also erode the agricultural base of affected communities, with documented income losses of 29–52% after irrigation infrastructure was destroyed ("Landslide Science and Practice," 2013), and nationally about 39% of buildings sit in non-zero susceptibility zones (Kincey et al., 2024b). This combination of high unpredictability and high consequences is what motivates susceptibility mapping as a planning tool rather than reactive, post-event response.

Landslide susceptibility mapping (LSM) classifies terrain by its relative likelihood of future failure, relating known landslides to the terrain conditions that characterise them (Reichenbach et al., 2018a). Unlike hazard or risk assessment, which adds temporal recurrence, exposure, and vulnerability, susceptibility addresses the more tractable question of where failure is relatively more or less likely (Guzzetti et al., 2005). That tractability makes susceptibility maps directly useful for land-use zoning, road maintenance prioritisation, early-warning design, and targeting scarce field investigation along a remote lifeline corridor like the Karnali Highway.

Susceptibility methods fall into three families (Aleotti & Chowdhury, 1999), (Reichenbach et al., 2018b). Heuristic (expert-based) methods rank factors by geomorphological judgement, often through multi-criteria or fuzzy-logic weighting, and are well represented in Nepal (Bijukchhen et al., 2013), (Pokharel & Gurung, 2024).

Statistical methods: frequency ratio, information value, weights-of-evidence, logistic regression, certainty factor, derive weights empirically from the observed association between landslides and each factor, and dominate the Nepali literature (Bhatta & Adhikari, 2024), (Devkota et al., 2013), (Kayastha et al., 2013), (Dahal & Hasegawa, 2008).

Physically based (deterministic) methods such as the infinite-slope model, TRIGRS, or SHALSTAB compute a factor of safety from geotechnical and hydrological first principles, offering mechanistic interpretability that empirical methods cannot (Woodard & Mirus, 2025a).

Each family has limitations that become acute in data-sparse, complex terrain like the Karnali corridor. Heuristic methods depend on analyst experience and are hard to validate objectively (Konakoglu & Kurt Konakoglu, 2025), (Feizizadeh et al., 2014).

Physically based methods need cohesion, friction angle, permeability, and bedrock-depth data that are rarely available at regional density, which limits consistent application over large areas (Woodard & Mirus, 2025b).

Classical statistical methods are reproducible but mostly assume linear or log-linear relationships and struggle with the non-linear, higher-order interactions that govern failure; they are also sensitive to mapping-unit and DEM-resolution choice, whose influence on derived geomorphometric factors remains poorly constrained (Chang et al., 2019).

Most importantly, none of these families routinely report where their predictions should be trusted: a susceptibility map assigns a value to every pixel or polygon with no statement of which predictions fall inside the conditions the model was built to represent (Meyer & Pebesma, 2021a).

Over the past decade, machine learning (ML) has displaced classical statistics as the dominant LSM approach, because tree- and kernel-based learners represent the non-linear interactions that logistic regression and frequency ratio cannot (Reichenbach et al., 2018c). Random Forest, SVMs, and gradient-boosted trees have been benchmarked widely: Random Forest was most accurate among four classifiers on the Karakorum Highway in northern Pakistan, a setting close to the Karnali corridor (Hussain et al., 2022); Random Forest and Linear Discriminant Analysis led a seven-model comparison at Abha Basin, Saudi Arabia (Youssef & Pourghasemi, 2021); and Random Forest reached 97% accuracy against a 298-site inventory in Wayanad, Kerala (P et al., 2025). Recent work has turned to tuned gradient boosting and Bayesian optimisation for further gains, including along the Karakoram Highway in Gilgit-Baltistan (Abbas et al., 2023).

A related development is ensemble modelling, which combines several base learners by averaging, stacking, or voting so that one model compensates for another's biases, as validated in Lombardy, Northern Italy (Xu et al., 2024). Ensembles formalise the variance-reduction argument of (Dietterich, 2000a) and show consistent, if resolution-dependent, gains over single models (Abraham et al., 2021) , (Lombardo et al., 2020) a pattern this study reproduces and examines in Section 4.

A third development is renewed attention to mapping units. Most ML-based LSM still uses regular pixels, but slope units: polygons bounded by ridgelines and valley lines that respect terrain structure; give more geomorphologically meaningful, decision-relevant zonation (Alvioli et al., 2016). Comparisons are mixed: a modified information-value study found slope units modestly outperformed grid cells (Ba et al., 2018), while a regional study in the Rwenzori Mountains found slope units especially useful where inventories are heterogeneous (Jacobs et al., 2020). Neither tested slope units against pixels across multiple kernel sizes with the same ensemble, the comparison undertaken here at 3×3, 15×15, and 25×25.

Across almost the entire ML-based LSM literature, performance is reported only through aggregate statistics: holdout AUC, F1, cross-validation accuracy, with no statement of where those statistics hold. ML models are interpolators: reliable within the feature space spanned by their training data and prone to degrade silently under extrapolation (Meyer & Pebesma, 2021b). A high cross-validation AUC describes skill inside the training feature space, not reliability in a neighbouring valley with a different lithology or drainage pattern.

The idea of bounding predictions has a longer history outside geoscience. In cheminformatics, the applicability domain of a QSAR model has for two decades been a mandatory companion to any prediction, limiting reliable predictions to inputs similar to the training set (Sahigara et al., 2012). Environmental modelling converged on an area of applicability based on a distance index in predictor space (Meyer & Pebesma, 2021c), and (Linnenbrink et al., 2026) showed that even spatial cross-validation remains optimistic under genuine extrapolation, so cross-validation alone cannot substitute for an explicit domain assessment.

LSM has been slow to adopt this layer despite needing it: Himalayan terrain has short-distance lithological and structural transitions, so a model trained on one unit can be asked, unnoticed, to extrapolate into terrain it never saw. This study treats the applicability domain not as an afterthought but as the mechanism that determines whether its multi-framework consistency finding can extend to comparable corridors. If susceptibility patterns replicate across three model families (RF, XGBoost, SVM), two mapping units, and three resolutions, that convergence indicates a terrain-driven signal rather than one model's inductive bias ; a claim only as strong as the domain layer that shows where the training data support it.

2 MATERIALS AND METHODS

2.1 STUDY AREA

The study region lies in the western hills and mountains of Nepal, mainly in Karnali Province and partly in Sudurpaschim, shown in Figure 1. It covers Kalikot District entirely and parts of Achham, Bajura, Jumla, and Dailekh, between 29°03′45″ and 29°24′10″ N and 81°27′30″ and 82°02′40″ E, about 2,155 km². Elevation ranges from 605 m in the southern valleys to 4,432 m in the northern mountains (mean 2,581 m).

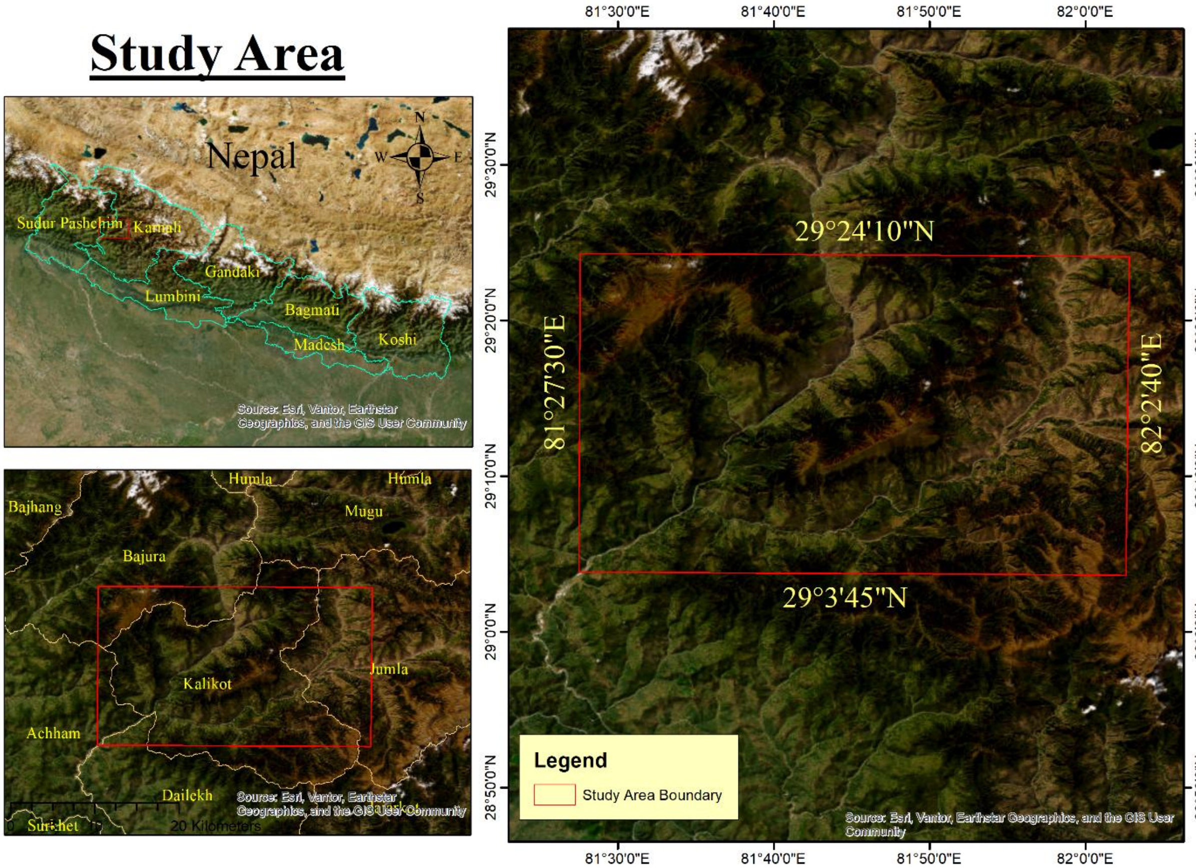

Figure 1: Study Area

The corridor sits within the greater Karnali River Basin. The Karnali Highway climbs from the Surkhet foothills toward Jumla along the Karnali and its tributaries, including the Tila; it is the main link between these remote districts and the rest of the country and closes for weeks during the monsoon from landslides, rockfall, and slope failure.

Geologically the area belongs to the Fore Himalaya and Midland zones of the Lesser Himalaya (Dhital, 2015), bounded to the north by the Main Central Thrust and to the south by the Main Boundary Thrust (Dhital, 2015), and built largely of low- to medium-grade metamorphic and metasedimentary rocks.

Climate varies strongly with the 605–4,432 m relief; the Indian summer monsoon and western disturbances supply most rainfall, though less than in eastern Nepal (Sahastrabuddhe et al., 2023). Steep slopes (commonly 30–45°), deep gorges, colluvial deposits, and active tectonics make this one of Nepal's more landslide-prone corridors (Dhital, 2015). The concentration of active failures along a lifeline road, together with an available inventory and high-resolution terrain and satellite data, motivated its selection.

2.2 *DATA USED*

2.2.1 *LANDSLIDE INVENTORY*

A landslide inventory was mapped over the 2,155 km² area by visual interpretation of high-resolution imagery, identifying landslides from scars, bare soil, disturbed vegetation, and lobate deposits and digitising them as polygons. Polygon mapping records both extent and source area (Mohammed et al., 2025) and has been applied across the data-sparse Himalaya (Batar & Watanabe, 2021); polygons carry more information per failure than single points (Godoy et al., 2022).

An equal number of non-landslide polygons were drawn over apparently stable terrain (gentle-to-moderate slopes, intact vegetation, no sign of past movement); because ML models need a binary target, negative-sample reliability matters as much as the positives, and poorly chosen negatives degrade accuracy (Gu et al., 2024).

For the pixel pipeline, 1,000 landslide and 1,000 non-landslide pixels were sampled per grid scale, giving a balanced 2,000-sample set per scale. Non-landslide pixels were drawn with a two-stage filter: a buffer around each mapped polygon excluded near-failure ground, and only pixels in Low or Very Low zones of a separate baseline susceptibility analysis were eligible, which lowers the chance of sampling genuinely unstable terrain as a negative. For the slope-unit pipeline, every unit containing a mapped landslide centroid was labelled positive and the rest negative, which yields naturally imbalanced sets (3x3: 278 landslide and 852 non-landslide, n = 1,130; 15x15 and 25x25: 338 and 507, n = 845). KML files were exported from Google Earth Pro and converted to shapefiles in QGIS.

2.2.2 *LANDSLIDE CONDITIONING FACTORS*

Eleven candidate factors were assembled; multicollinearity screening (Section 2.3.1) removed two, leaving nine used in all modelling and listed with the inventory in Table 1. Factors were chosen for their documented influence on landslides across topography, hydrology, geology, and proximity to natural and built features.

Table 1: Category, Source Derivation and Units for Landslide Conditioning Factors

Factor	Category	Source / Derivation	Unit
Slope	Topographic	ALOS PALSAR 12.5 m DEM derivative	Degrees
Aspect	Topographic	ALOS PALSAR 12.5 m DEM derivative	Degrees
Curvature (profile)	Topographic	ALOS PALSAR 12.5 m DEM derivative	1/m
Topographic Wetness Index	Hydrological	ALOS PALSAR 12.5 m DEM derivative	Dimensionless
Distance to fault	Geological	DMG structural geology map (1:400,000)	Metres
Distance to thrust	Geological	DMG structural geology map (1:400,000)	Metres
NDVI	Land cover	Sentinel-2 L2A, 10 m (2021-2024 dry-season minimum)	Dimensionless
Distance to road	Anthropogenic	Euclidean distance from road network	Metres

Distance to river	Hydrological	Euclidean distance from DEM-derived stream network	Metres

a) *Topographic Factors*

Topography strongly governs slope stability, runoff, and erosion (McColl, 2022); the topographic factors are slope, aspect, profile curvature, and the topographic wetness index (TWI), all derived from the DEM.

Steeper slopes are less stable (Nath et al., 2021); slope was computed from the DEM using the gradient approach of (Keles & Nefeslioglu, 2021):

$$Slope(\theta) = \arctan\sqrt{(\frac{\partial z}{\partial x})^2 + (\frac{\partial z}{\partial y})^2}$$

where, $\partial z/\partial x$ and $\partial z/\partial y$ are the rates of change of elevation in the x and y directions. Most terrain lies in the 16–48° range, and landslides concentrate in these moderate-to-steep zones, consistent with slope angle as a primary control on shear stress.

Aspect sets slope orientation, which affects insolation, vegetation, and weathering (Galli et al., 2008). Mapped landslides occur across all aspect classes, with somewhat greater representation on south- to south-west-facing slopes; a pattern echoed by the later feature-importance and SHAP results.

The topographic wetness index (TWI) combines slope and upstream contributing area (W. Chen et al., 2017) (Roy & Saha, 2019):

$$TWI = \ln(\frac{A_S}{\tan(\theta)})$$

Here $\tan(\theta)$ is the slope gradient and A_s the upstream contributing area. TWI indicates where water accumulates and soil cohesion may fall; values are mostly low-to-moderate given the steep, well-drained terrain, but high-TWI drainage hollows coincide with several landslide clusters.

Profile curvature, the curvature in the vertical plane along the slope (Yilmaz et al., 2012), is near-zero across most of the area (−0.0004 to 0.0181), so curvature alone is not a dominant control but contributes with other factors.

The topographic layers are shown in Figure 2.

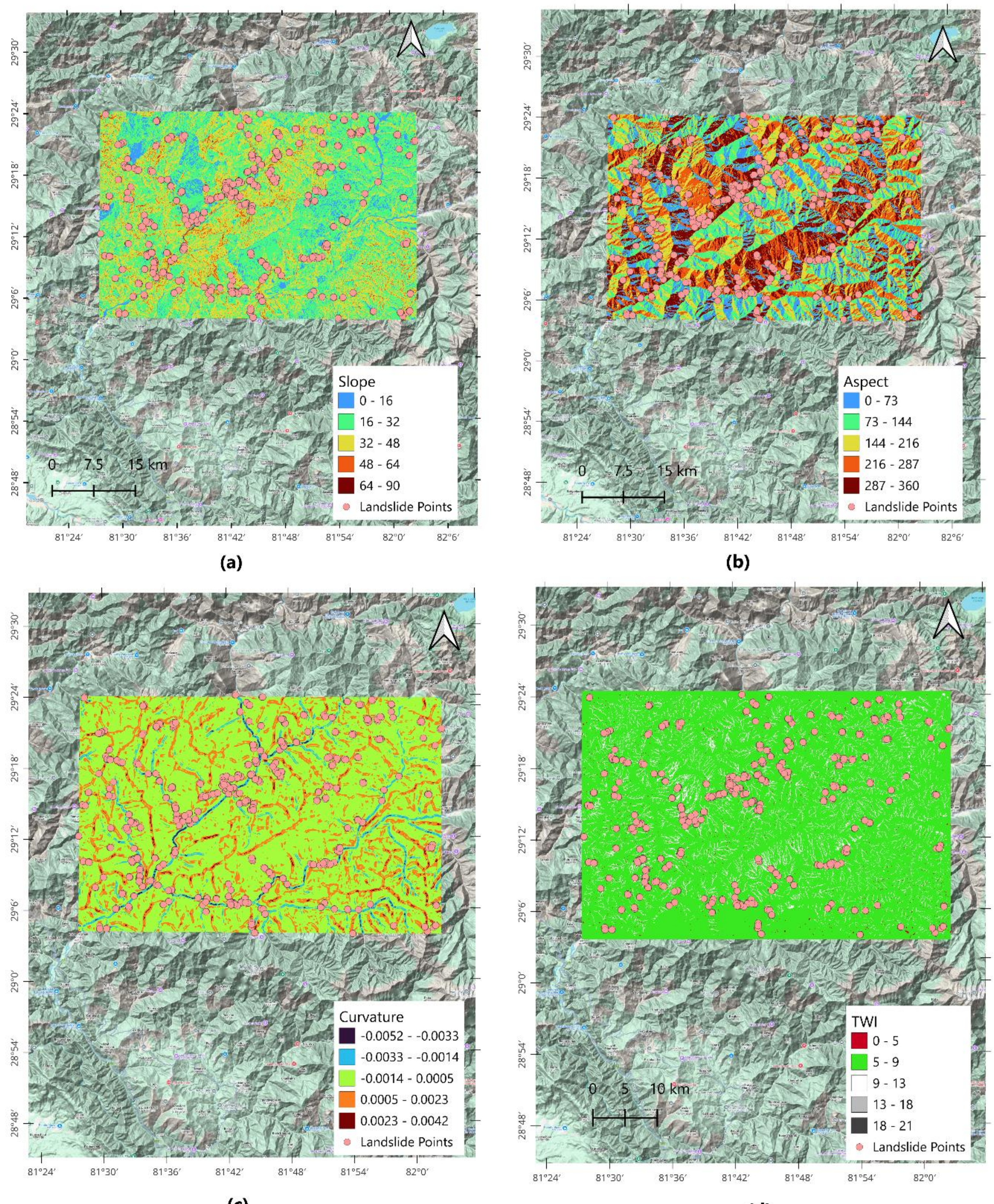

Figure 2: Maps Showing Landslide Conditioning – Topographical Factors: (a) Slope, (b) Aspect, (c) Profile Curvature and (d) TWI

b) *Land Cover Factors*

Vegetation density was quantified with NDVI (Choi et al., 2012), computed from the red and infrared Sentinel-2 L2A bands:

$$NDVI = \frac{IR - R}{IR + R}$$

where R and IR are the red and infrared reflectance.

In Figure 3, NDVI is classified into five ranges from ≤ −0.6 (bare rock and snow) to > 0.6 (dense vegetation). Most of the area carries moderate-to-dense cover (NDVI 0.2–0.6), typical of forested mid-hill slopes, with lower values along valley corridors, ridgelines, and disturbed ground. Many landslides cluster in moderate-NDVI rather than densely vegetated zones, consistent with root reinforcement stabilising steep terrain and its loss raising failure risk.

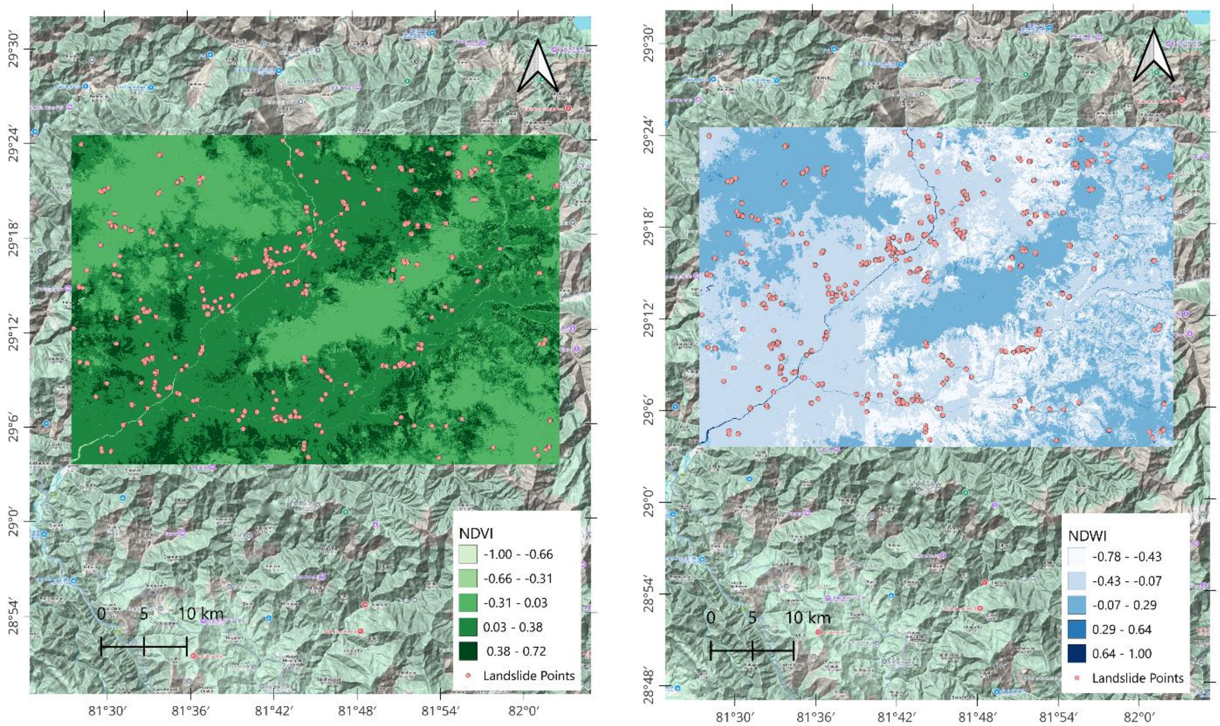

a

b

Figure 3: Map Showing Landslide Conditioning – Land Cover Factor: (a) NDVI and (b) NDWI

c) *Proximity to anthropogenic and natural features*

Four proximity factors were computed by Euclidean distance: distance to river and road from hydrological and road networks, and distance to thrust and fault from thrust and faults in geological maps and tectonic databases. Fracturing, shear zones, and reduced rock-mass integrity near faults and thrusts raise vulnerability, and proximity to these structures also promotes seepage and seismic amplification.

Landslides concentrate in the nearest class of each factor (shown in Figure 4): ≤ 4,876 m for faults, ≤ 270 m for rivers the strongest single proximity association and ≤ 1,073 m for roads, while thrust proximity shows a broader, less localised influence.

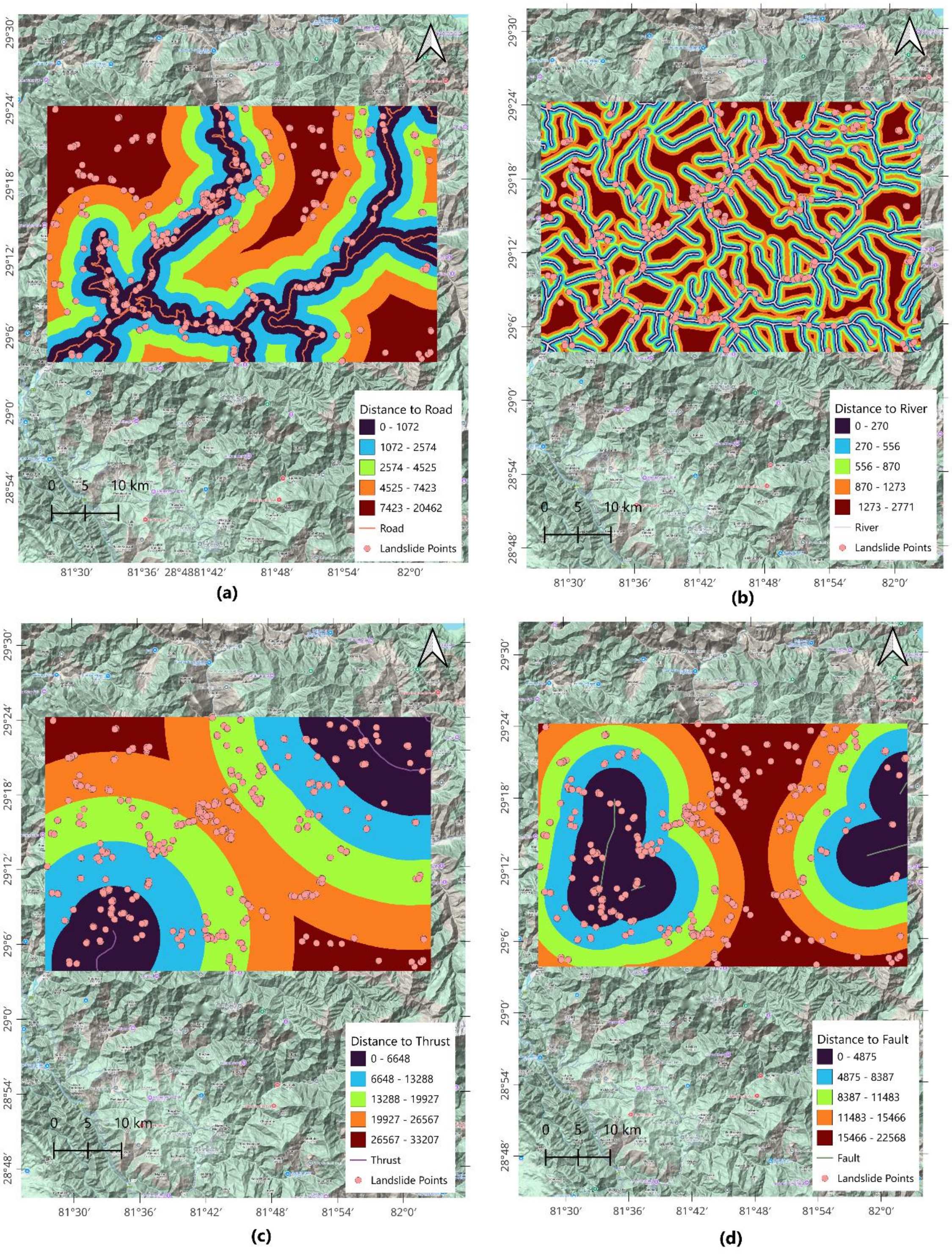

Figure 4: Map Showing Landslide Conditioning – Anthropogenic Factors: **(a)** Distance to Road, **(b)** Distance to River, **(c)** Distance to Thrust, and **(d)** Distance to fault

2.2.3 *MULTI-SCALE SPATIAL GRID DESIGN*

Conditioning-factor statistics were examined at three grid resolutions: 3×3, 15×15, and 25×25 pixels; representing fine, medium, and coarse aggregation. Factor values at each sample site were taken from the corresponding spatial-averaging window.

2.3 *METHODS*

The framework (Figure 5) is a sequential pipeline: data pre-processing; exploratory analysis; train–test splitting; Bayesian hyperparameter optimisation with inner cross-validation; probability calibration; evaluation; SHAP interpretability; ensemble construction; pixel-wise raster prediction; and applicability-domain assessment. It was implemented in Python 3.10 (scikit-learn 1.3, XGBoost 1.7, SHAP 0.42, scikit-optimize 0.9, rasterio 1.3, joblib 1.3) on Google Colaboratory with GPU disabled for determinism.

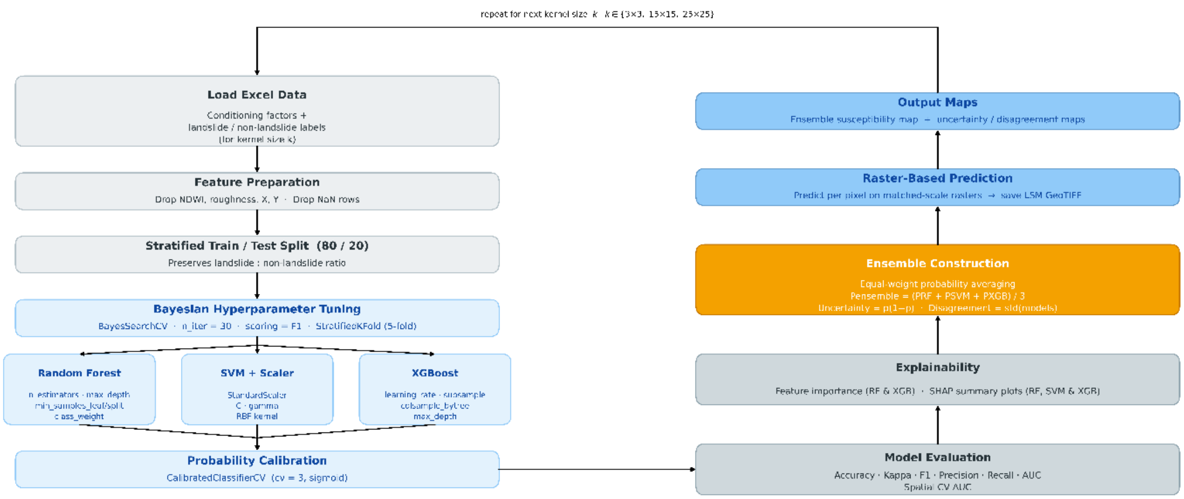

Figure 5: Methodological framework for landslide susceptibility modelling

2.3.1 *DATA PRE-PROCESSING*

Factor tables were read by Excel and cleaned. Of the eleven candidates, two were dropped for collinearity: NDWI (McFeeters, 1996), a dry-season maximum composite from the same Sentinel-2 imagery, correlated with NDVI (|r| = 0.83), and terrain roughness correlated with slope (|r| = 0.96). The more interpretable factor was kept in each pair (NDVI and slope), leaving nine with no remaining pair above the |r| > 0.8 threshold. Rows with nulls were dropped. Correlation heatmaps and per-class kernel-density plots compared landslide and non-landslide distributions.

2.3.2 *PIXEL-BASED APPROACH WITH MULTI-SCALE ZONAL STATISTICS*

Conditioning-factor values were extracted with square moving-window kernels of 3×3, 15×15, and 25×25 pixels. Multiple window sizes reflect the multi-scale nature of hillslope processes: small windows capture local conditions relevant to shallow translational failures; larger windows integrate neighbourhood context relevant to deeper rotational failures. For each window, the meaning of each factor was recorded as the feature vector.

2.3.3 *SLOPE UNIT-BASED APPROACH*

Slope units were delineated with the r.slopeunits module in GRASS GIS, which partitions terrain into hydrologically coherent units bounded by ridgelines and valley lines while enforcing internal aspect homogeneity, controlled by a minimum area threshold (a) and a circular variance (c). A grid search over six values of a (50,000–300,000 m^2, step 50,000) and seven of c (0.10–0.40, step 0.05) gave 42 configurations, each evaluated with a Global Heterogeneity index (GH) combining normalised global aspect variance (V, intra-unit homogeneity) and weighted Moran's index (wMI, inter-unit heterogeneity), where lower GH is better. GH ranged from 0.9996 to 1.0440; the minimum (0.9996, at a = 300,000 m^2 and c = 0.35) yielded 9,952 polygons (V = 0.7400, wMI = 0.9996) and was selected as optimal.

2.3.4 *DATA SPLITTING AND CROSS-VALIDATION STRATEGY*

Pixel datasets used an 80/20 stratified split with spatial grouping on 1,000 m blocks to limit leakage between nearby observations. Within the training data, five-fold StratifiedGroupKFold used the same 1,000 m blocks as groups while preserving class balance during tuning.

For slope units, centroids were assigned to 2,000 m blocks, and StratifiedGroupKFold with the same 2,000 m blocking was used for both the outer 80/20 holdout and the inner five-fold tuning. This spatially blocked design reduces the optimistic bias that arises when adjacent observations fall in both training and validation folds.

2.3.5 *BAYESIAN HYPERPARAMETER OPTIMISATION*

Grid and random search are inefficient in high-dimensional spaces. Bayesian optimisation (Snoek et al., 2012) builds a probabilistic surrogate of the objective and uses an acquisition function to choose the next query, balancing exploration and exploitation. BayesSearchCV (scikit-optimize) ran 20 iterations per model per grid scale, optimising F1-score for balanced performance under class imbalance; search spaces are in Table 2.

Table 2: Hyperparameter search spaces for RF, SVM, and XGBoost (Bayesian optimisation).

Model	Hyperparameter	Search Space	Type
Random Forest	n_estimators	[150, 400]	Integer
Random Forest	max_depth	[5, 25]	Integer
Random Forest	min_samples_split	[2, 10]	Integer
Random Forest	min_samples_leaf	[1, 10]	Integer
Random Forest	class_weight	balanced / balanced_subsample	Categorical
SVM	C	[0.01, 100] (log-uniform)	Real
SVM	Gamma	[1e-5, 10] (log-uniform)	Real
SVM	Kernel	rbf	Categorical
XGBoost	n_estimators	[150, 400]	Integer

XGBoost	max_depth	[3, 12]	Integer
XGBoost	learning_rate	[0.01, 0.3] (log-uniform)	Real
XGBoost	Subsample	[0.6, 1.0]	Real
XGBoost	colsample_bytree	[0.6, 1.0]	Real

For SVM, a Pipeline wrapping StandardScaler and SVC ensured scaling fit within each fold, preventing leakage into the scaler statistics (Kaufman et al., 2012).

2.3.6 *MACHINE LEARNING MODELS*

a) *Random Forest (RF)*

Random Forest is a bagging ensemble of decision trees, each on a bootstrap sample with random feature subsets at each split, which decorrelates trees and reduces variance (Breiman, 1996); n_estimators, max_depth, min_samples_split, min_samples_leaf, and class_weight (balanced / balanced_subsample) were tuned.

b) *Support Vector Machine*

The SVM used a radial-basis kernel (Cortes & Vapnik, 1995), embedded in a StandardScaler pipeline, with C and gamma optimised over log-uniform ranges and class_weight='balanced'.

c) *XGBoost (XGB)*

XGBoost builds gradient-boosted trees with a second-order loss expansion and L1/L2 regularisation (T. Chen & Guestrin, 2016); n_estimators, max_depth, learning_rate, subsample, and colsample_bytree were tuned under a binary:logistic objective with log-loss.

2.3.7 *PROBABILITY CALIBRATION*

Raw scores from the three models are not comparable: RF vote aggregation is bimodal toward 0 and 1, XGBoost overestimates high probabilities under imbalance, and SVM predict_proba clusters near 0.4–0.6, understating certainty. Naive averaging would discount SVM and make inter-model agreement uninterpretable.

Platt scaling was therefore fit independently for each model on out-of-fold predictions from the spatially blocked folds, remapping each score to a posterior P (landslide | x) on a common axis. Because the Platt sigmoid is monotonic, calibration preserves rank order and leaves AUC essentially unchanged, so post-calibration divergence reflects genuine uncertainty rather than score-range differences: a prerequisite for the Mahalanobis applicability domain.

In the slope-unit pipeline, Platt scaling was fit on roughly 700 polygons per fold, so individual slope-unit probabilities are approximate, though calibration still improves cross-model comparability and the ensemble and domain assessments remain valid.

2.3.8 *FEATURE IMPORTANCE AND SHAP ANALYSIS*

Feature importance used three approaches: native Gini importance for RF and XGBoost; permutation importance (10 repetitions, mean F1 decrease) for SVM; and permutation importance on the ensemble mean probability. Global SHAP summary plots were generated for all base models (TreeExplainer for RF and

XGBoost, KernelExplainer for SVM with a 100-instance background), with beeswarm plots showing the magnitude and direction of each factor's effect (Lundberg & Lee, 2017).

2.3.9 *Ensemble Construction*

The ensemble model combines the calibrated predictions of RF, SVM, and XGBoost through arithmetic mean probability averaging:

$$P\ ensemble\ (x) = \left(\frac{1}{3}\right) * [P_{RF(x)} + P_{SVM} + P_{XGB(x)}]$$

A binary prediction is obtained at a 0.5 threshold. Averaging reduces variance in proportion to the pairwise correlation between base classifiers (Dietterich, 2000b) and improves consistently on individual models in LSM settings (V. T. Nguyen et al., 2019). The ensemble bundle (three calibrated models, feature list, threshold, and aggregation method) was serialised with joblib for raster prediction.

2.3.10 *Pixel-wise Susceptibility Mapping*

The ensemble was applied across the study area using co-registered raster stacks loaded with rasterio, with a validity mask for finite, non-nodata pixels and feature order preserved from training. Probability maps were reshaped to the raster grid and written as LZW-compressed GeoTIFFs.

2.3.11 *Applicability Domain Assessment*

The applicability domain (AD) framework assesses whether each prediction pixel falls within the feature space represented by the training data, and whether the three base models agree on their predictions. The domain score is computed as:

$$d(x) = \sqrt{(x-\mu)^T \boldsymbol{\Sigma}^{-\mathbf{1}} (\boldsymbol{x}-\mu)}$$

$$Domain\ Score(x) = 1 - clip(\frac{d(x)}{d_{95}}, 0{,}1)$$

where μ is the training feature mean vector, Σ^{-1} the precision matrix estimated by Ledoit & Wolf well-conditioned even when features approach samples (Ledoit & Wolf, 2004) — and d_{95} the 95th-percentile training Mahalanobis distance used as the threshold.

The model agreement score is computed as

$$Agreement\ Score(x) = 1 - clip(\frac{STD(P_{RF}, P_{SVM}, P_{XGB})}{0.5}, 0{,}1)$$

, where 0.5 represents the maximum possible standard deviation of three probabilities bounded in [0,1].

3 RESULTS

3.1 *FEATURE CORRELATION AND SELECTION*

Pearson correlation among the eleven candidates (Figure 6) showed most pairs weakly correlated ($|r| < 0.2$). Two exceeded the threshold: roughness–slope ($r = 0.97$), where roughness was dropped for slope, and NDVI–NDWI ($r = -0.83$), where NDWI was dropped for the more relevant NDVI. Distance to road–thrust ($r = 0.48$) and fault–thrust ($r = 0.43$) were moderate and retained. The nine retained factors: aspect, profile curvature, distance to fault, river, road, and thrust, NDVI, slope, and TWI, carried forward with reduced redundancy.

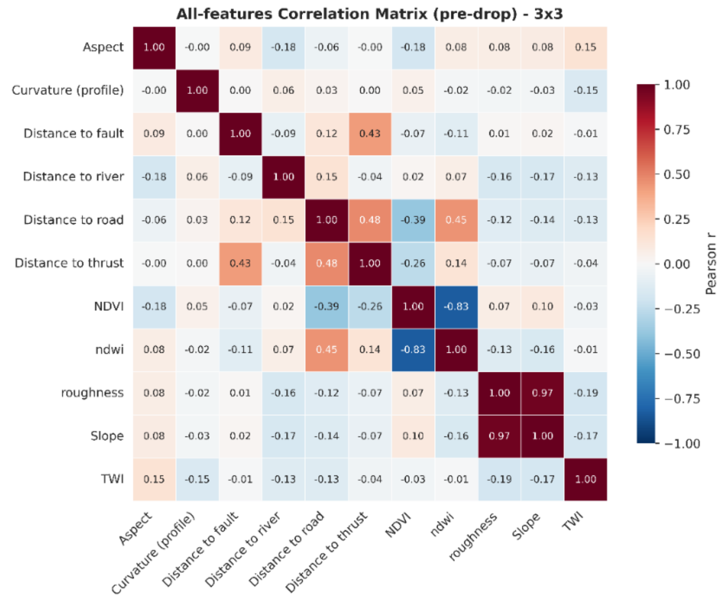

Figure 6: Correlation matrix of conditioning factors before feature selection.

3.2 *PIXEL-BASED MODEL PERFORMANCE*

Across the three resolutions, the 15×15 grid gave the highest performance for every classifier. XGBoost was best overall (AUC = 0.9930, CV AUC = 0.9816 ± 0.0102, accuracy 96.6%, F1 = 0.965), with the 15×15 ensemble close behind (AUC = 0.9894, 95.6%). Performance fell at 25×25, most for RF (AUC = 0.9617), while XGBoost stayed most robust. Spatial CV AUCs tracked holdout AUCs with low spread, indicating robust spatial generalisation and little overfitting.

Table 3: Classification performance metrics for pixel-based models across three spatial window sizes.

Grid	Model	AUC (Holdout)	CV AUC (Spatial)	Accuracy	Precision	Recall	F1
3×3	RF	0.9601	0.9791 ± 0.0055	92.2%	0.907	0.918	0.913
3×3	SVM	0.9636	0.9647 ± 0.0050	90.8%	0.914	0.874	0.894
3×3	XGB	0.9719	0.9844 ± 0.0026	93.1%	0.924	0.918	0.921
3×3	Ensemble	0.9676	—	92.8%	0.924	0.912	0.918

15×15	RF	0.9895	0.9790 ± 0.0085	93.6%	0.923	0.950	0.937
15×15	SVM	0.9729	0.9677 ± 0.0139	91.2%	0.919	0.901	0.910
15×15	XGB	0.9930	0.9816 ± 0.0102	96.6%	0.970	0.960	0.965
15×15	Ensemble	0.9894	—	95.6%	0.951	0.960	0.956
25×25	RF	0.9617	0.9748 ± 0.0087	89.6%	0.895	0.885	0.890
25×25	SVM	0.9542	0.9608 ± 0.0040	89.9%	0.874	0.920	0.896
25×25	XGB	0.9776	0.9801 ± 0.0085	92.6%	0.930	0.914	0.922
25×25	Ensemble	0.9702	—	92.1%	0.929	0.902	0.915

3.2.1 *ROC-AUC COMPARISON ACROSS RF, XGBOOST, AND SVM*

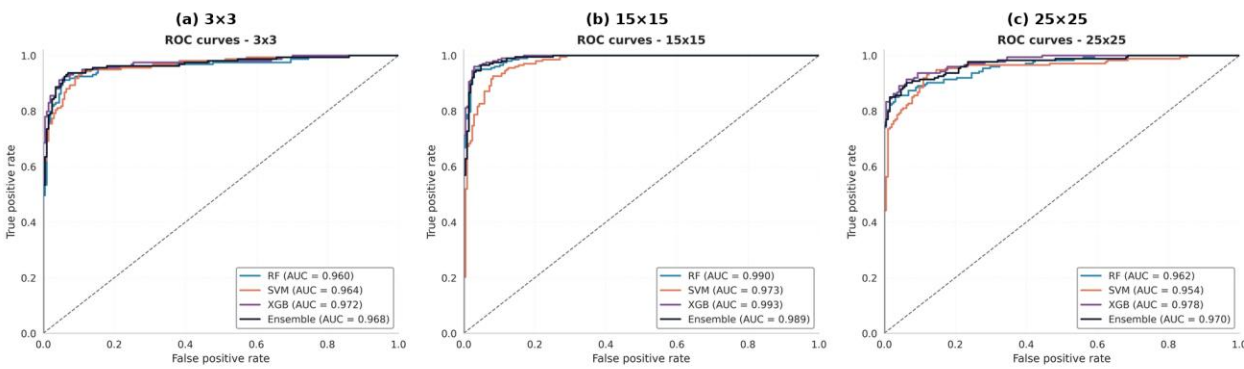

Figure 7: Receiver Operating Characteristic (ROC) curves comparing the performance of Random Forest (RF), Support Vector Machine (SVM), XGBoost (XGB), and an Ensemble model across three input matrix sizes: (a) 3×3, (b) 15×15, and (c) 25×25.

The ROC curves (Figure 7) match the metrics: XGBoost led at every resolution (0.972 at 3×3, 0.993 at 15×15, and 0.978 at 25×25), all models exceeded 0.960 at 3×3 and 0.954 at 25×25, and the 15×15 curves were steepest and most tightly clustered.

3.3 ***SLOPE UNIT-BASED MODEL PERFORMANCE***

Slope-unit models, with per-model threshold optimisation (Table 4), performed below their pixel counterparts. XGBoost led at 3×3 (AUC = 0.907, F1 = 0.679) and the ensemble at 15×15 (AUC = 0.870, F1 = 0.752); performance fell at 25×25, where SVM gave the lowest AUC (0.762). Spatial CV AUCs was stable (±0.011 to ±0.029) and thresholds varied (0.30–0.44).

Table 4: Classification performance metrics for slope unit-based models.

Grid	**Model**	**Threshold**	**AUC (Holdout)**	**CV AUC (Spatial)**	**Accuracy**	**Precision**	**Recall**	**F1**
3×3	RF	0.37	0.8920	0.8819 ± 0.0215	79.6%	0.567	0.654	0.607

3×3	SVM	0.30	0.8444	0.8632 ± 0.0252	78.7%	0.543	0.731	0.623
3×3	XGB	0.37	0.9069	0.8787 ± 0.0216	84.3%	0.667	0.692	0.679
3×3	Ensemble	0.41	0.8864	—	83.3%	0.648	0.673	0.660
15×15	RF	0.33	0.8532	0.8572 ± 0.0154	78.3%	0.686	0.842	0.756
15×15	SVM	0.44	0.8551	0.8375 ± 0.0223	77.6%	0.705	0.754	0.729
15×15	XGB	0.30	0.8565	0.8561 ± 0.0111	76.2%	0.653	0.860	0.742
15×15	Ensemble	0.36	0.8695	—	78.3%	0.691	0.825	0.752
25×25	RF	0.43	0.8089	0.8655 ± 0.0225	69.9%	0.603	0.641	0.621
25×25	SVM	0.38	0.7616	0.8604 ± 0.0220	69.9%	0.597	0.672	0.632
25×25	XGB	0.34	0.8261	0.8645 ± 0.0287	73.5%	0.647	0.688	0.667
25×25	Ensemble	0.38	0.8032	—	70.5%	0.609	0.656	0.632

3.3.1 *ROC-AUC comparison across RF, XGBoost, and SVM*

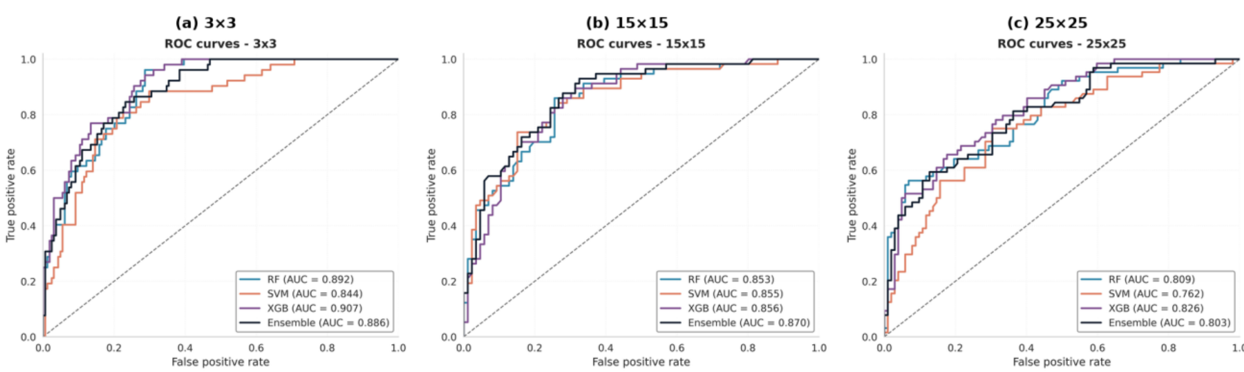

Figure 8: Receiver Operating Characteristic (ROC) curves comparing the performance of Random Forest (RF), Support Vector Machine (SVM), XGBoost (XGB), and an Ensemble model across three input matrix sizes: (a) 3×3, (b) 15×15, and (c) 25×25.

The slope-unit ROC curves (Figure 8) confirm the lower discrimination, with stepped, irregular shapes reflecting smaller effective samples and greater within-unit heterogeneity, so pixel-based approaches discriminate better in this study area.

3.4 *FREQUENCY RATIO VALIDATION OF SUSCEPTIBILITY CLASSES*

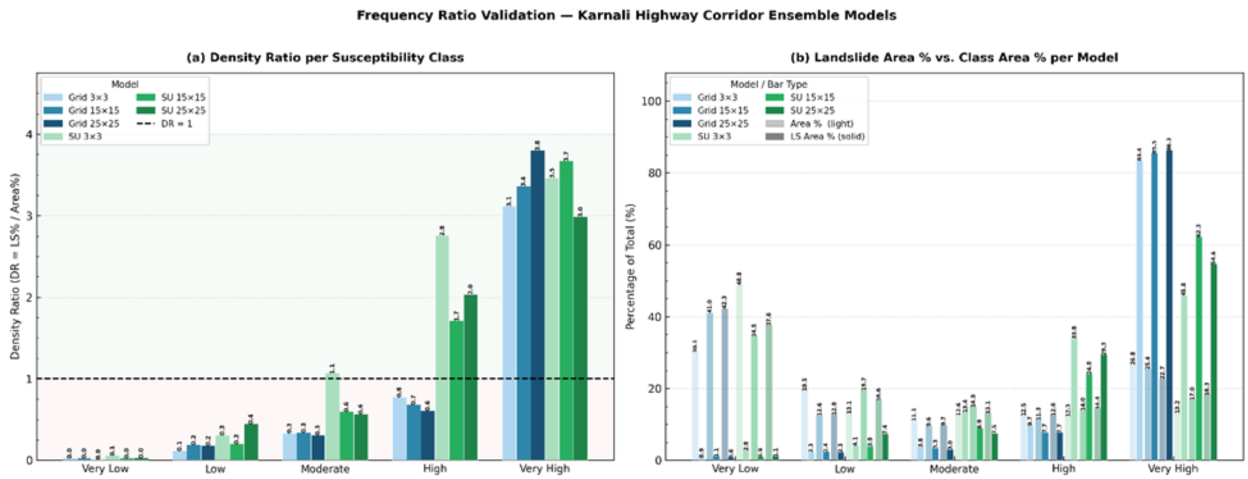

Figure 9: Frequency ratio (density ratio, DR) validation of Jenks-classified susceptibility maps for grid-based and slope-unit ensemble models across 3×3, 15×15, and 25×25 kernel resolutions.

Frequency-ratio (density-ratio, DR) analysis gave monotonically increasing DR from Very Low to Very High across all six ensemble models and both mapping units, with no inversions (Figure 9). Grid-based models discriminated most strongly, their Very High class capturing 83.4–86.3% of landslide area over 22.7–26.8% of the corridor (DR 3.12–3.80). Slope-unit models showed a moderate concentration, their Very High class capturing 45.8–62.3% of landslide area (DR 2.99–3.67); the lower absolute concentration reflects polygon smoothing, not reduced skill, since per-unit-area DR is comparable. In both pipelines the 15×15 kernel gave the highest Very High DR (grid 3.36, slope unit 3.67), corroborating it as optimal, while the Very Low class held DR below 0.04 and under 1% of landslide area over 30–42% of the corridor.

3.5 *FEATURE IMPORTANCE AND SHAP ANALYSIS*

RF and XGBoost importance rankings (Table 5) converged on the same top predictors, with aspect first by a clear margin, then NDVI, slope, and TWI; distance to thrust, road, river, and fault occupied the middle ranks and profile curvature least. The agreement indicates the hierarchy is robust to model-specific bias.

Table 5: Top 10 conditioning factors ranked by RF and XGB feature importance, with geomorphological interpretations

Rank	Factor	RF importance	XGB importance
1	Aspect	0.385	0.335
2	NDVI	0.137	0.118
3	Slope	0.101	0.129
4	TWI	0.099	0.103

5	Distance to thrust	0.077	0.095
6	Distance to road	0.071	0.076
7	Distance to river	0.059	0.074
8	Distance to fault	0.039	0.044
9	Curvature (profile)	0.031	0.027

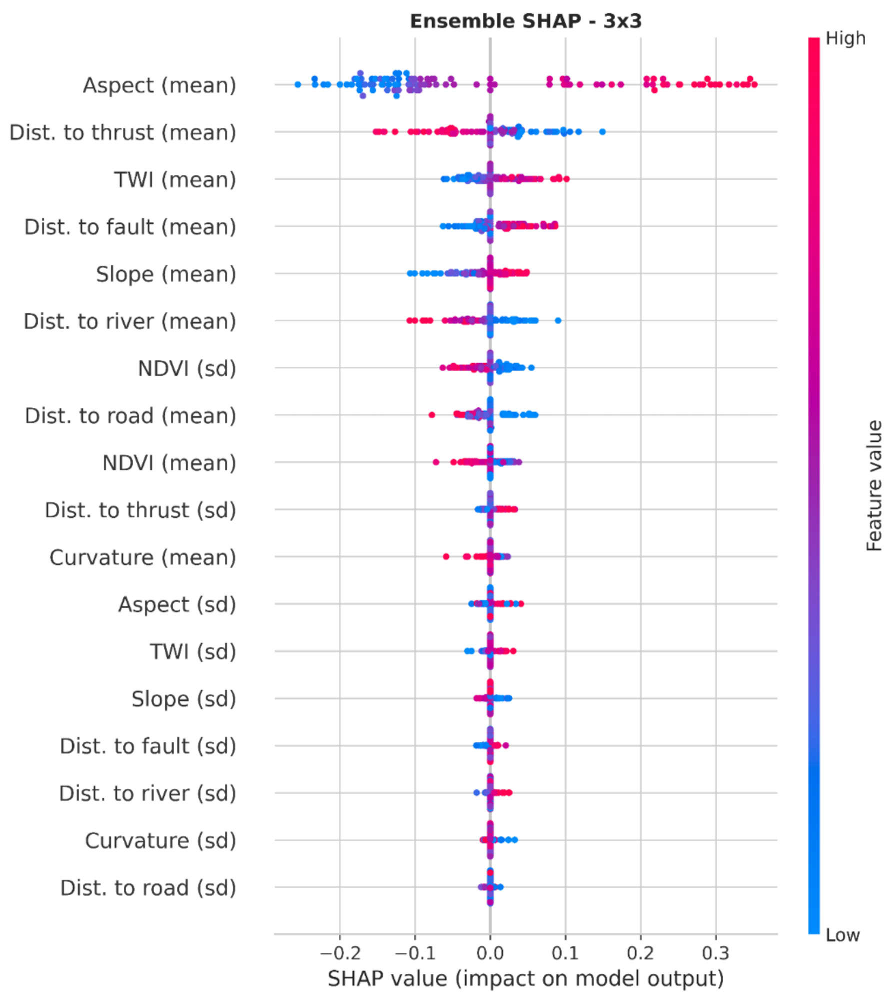

Figure 10: SHAP summary plots for the 3×3 grid-based models

SHAP summary plots for the 3×3 grid-based ensemble (Figure 10) added direction to magnitude. High slope, low distance-to-fault, and high TWI gave the largest positive contributions, while high NDVI gave negative contributions, confirming the protective role of dense vegetation. Aspect was important, with higher susceptibility associated mainly with south- to southwest-facing slopes, plausibly reflecting monsoonal moisture exposure, though this is a model-derived association rather than direct causation. Profile curvature showed the narrowest spread. The patterns were consistent across the other resolutions and slope-unit configurations, so the 3×3 results are representative.

3.6 *LANDSLIDE SUSCEPTIBILITY MAPS*

a) *Pixel Based Approach*

Pixel-based maps were produced at all three window sizes, classified Very Low to Very High from the ensemble of RF, SVM, and XGB, with warmer colours indicating higher susceptibility.

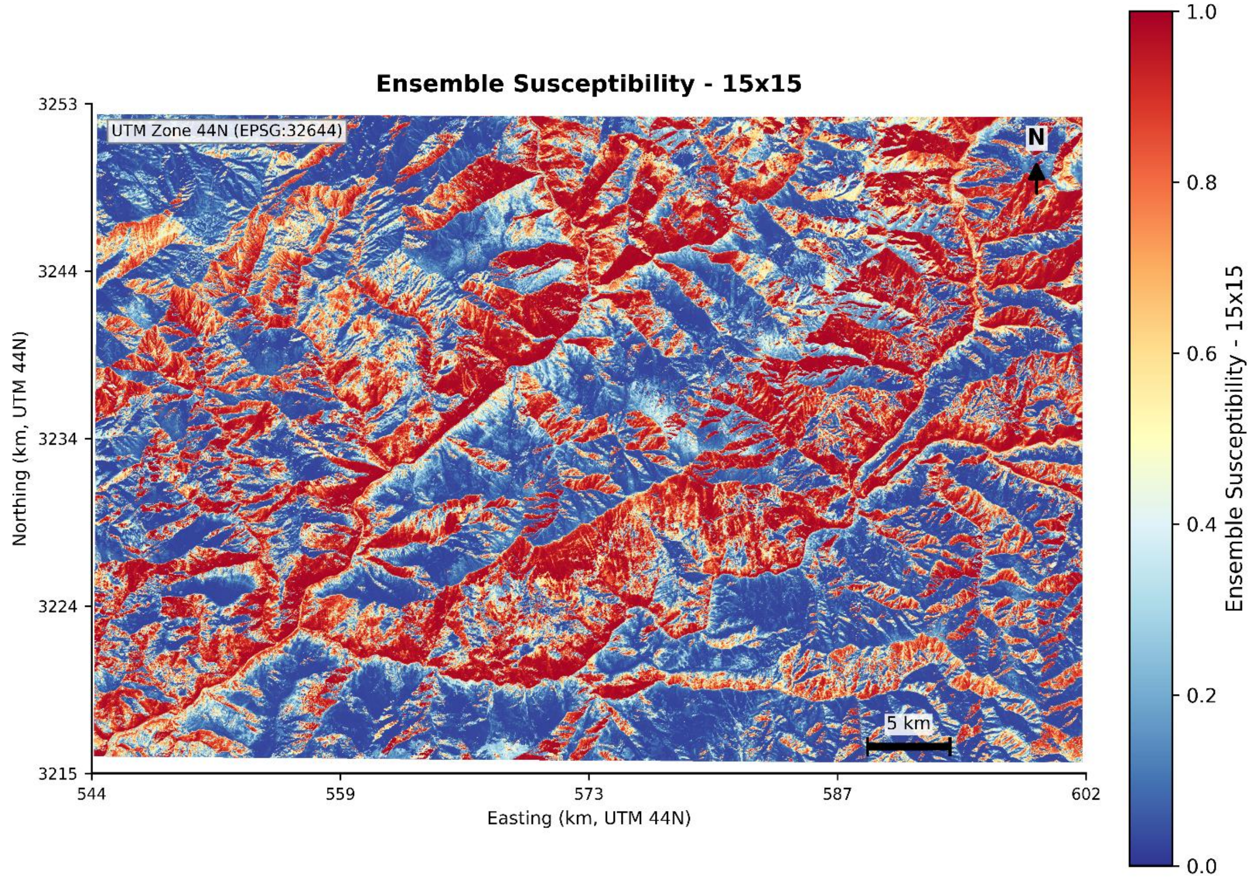

*Figure 11: Grid-based (15×15) landslide susceptibility maps generated using **RF**, **SVM**, **XGB**, and **Ensemble** models*

The 15×15 ensemble map (Figure 11) shows a spatially coherent pattern, with Very High and High zones along steep escarpments, structurally controlled ridgelines, and drainage-adjacent facets in the central and north-western corridor. About 37% of the corridor is High or Very High. The 15×15 kernel captures terrain context at a scale consistent with characteristic Himalayan hillslope lengths, giving a surface neither fragmented at fine scales nor over-smoothed at coarse ones.

b) *Slope Unit Based Approach*

Slope-unit maps were produced at the same window sizes, each panel showing RF, SVM, XGB, and the ensemble over hydrologically defined polygons, producing a ridge-and-valley mosaic that reflects the terrain's geomorphological boundaries.

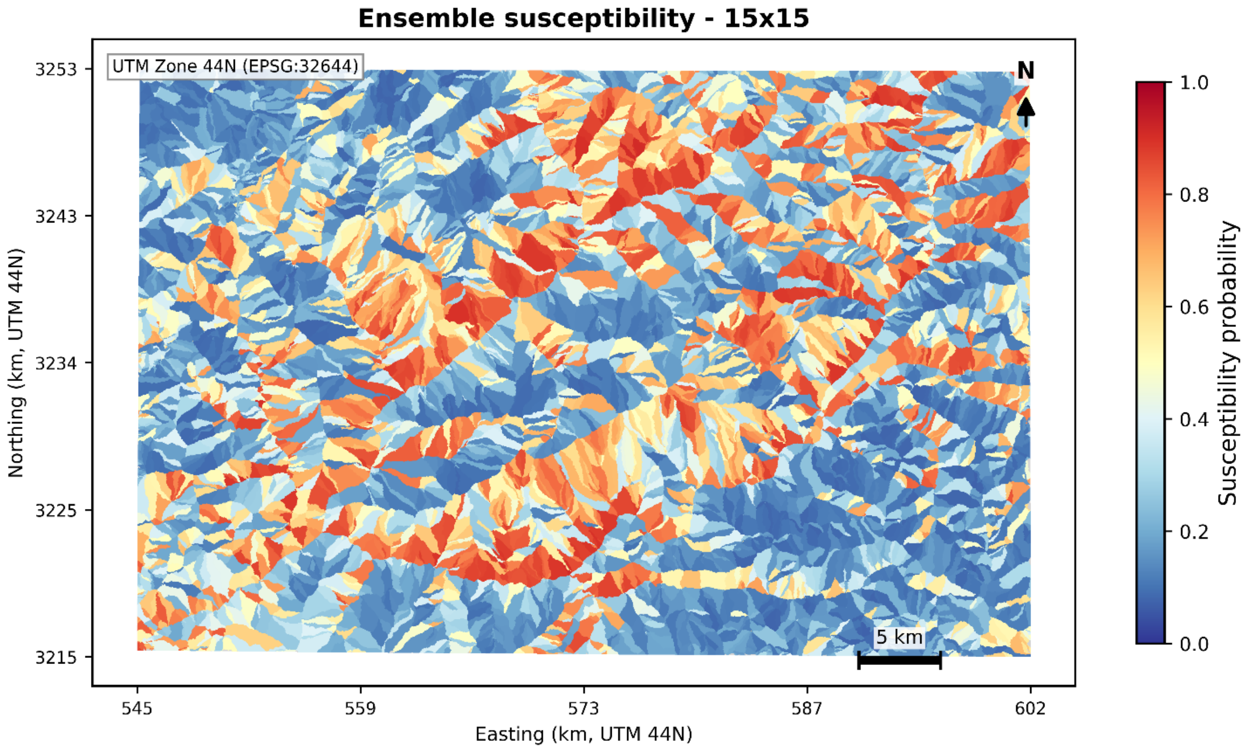

Figure 12: Slope unit-based (15×15) landslide susceptibility maps generated using ***RF****,* ***SVM****,* ***XGB****, and* ***Ensemble*** *models*

The 15×15 slope-unit ensemble map (Figure 12) conveys the same signal through the polygon mosaic, with high-susceptibility polygons on steep structurally controlled facets and drainage-adjacent units, matching the pixel pattern. The delineation is directly usable for infrastructure risk zoning, since slope-unit boundaries follow the features that define exposure for roads and settlements rather than arbitrary grid cells.

3.7 *APPLICABILITY DOMAIN RESULTS*

The AD mask identifies a large, well-separated trusted zone at every resolution and for both mapping units. At the 0.5 threshold, trusted coverage exceeded 97% for grids (97.54%, 97.62%, 97.60% at 3×3, 15×15, 25×25) and 98% for slope units (98.41%, 99.11%, 98.75%), retaining most of the area while flagging only a small uncertain fraction.

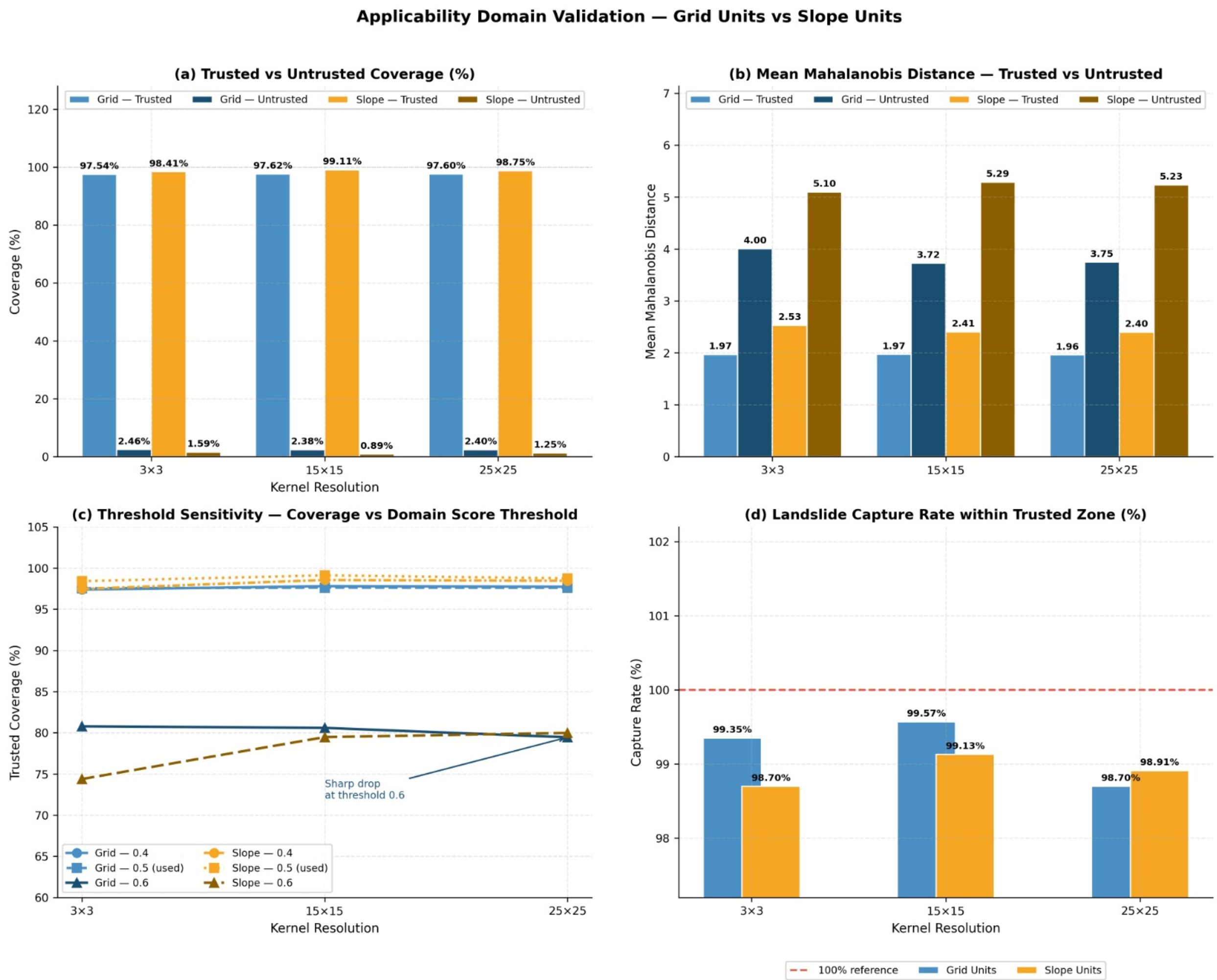

Figure 13: Applicability domain validation of grid and slope-unit models at different kernel resolutions (3×3, 15×15, and 25×25).

Table 6: Summary of applicability domain validation metrics for grid-based and slope-unit landslide susceptibility models across different kernel resolutions (3×3, 15×15, and 25×25).

Resolution	**Grid Based**			**Slope Unit Based**		
	3x3	15x15	25x25	3x3	15x15	25x25
Total_Valid_Pixels	236009064	9372074	3317601	3417462	3417462	3417462
Trusted_Pixels	230201953	9149316	3238127	3363116	3387197	3374769
Trusted_Coverage_pct	97.54	97.62	97.6	98.41	99.11	98.75
Untrusted_Pixels	5807111	222758	79474	54346	30265	42693
Untrusted_Coverage_pct	2.46	2.38	2.4	1.59	0.89	1.25
Mean_Ensemble_Susc_Trusted	0.4309	0.4151	0.4003	0.2921	0.3944	0.3814
Mean_Ensemble_Susc_Untrusted	0.4613	0.4768	0.5077	0.4259	0.4217	0.4371
Mean_Mahal_Dist_Trusted	1.9686	1.9702	1.959	2.5285	2.4053	2.399
Mean_Mahal_Dist_Untrusted	4.0038	3.7247	3.7463	5.0952	5.2871	5.2341
Mean_Disagree_Std_Trusted	0.0768	0.0743	0.0838	0.0604	0.0632	0.0607

Mean_Disagree_Std_Untrusted	0.1874	0.2344	0.2208	0.1185	0.0831	0.0748
Mean_Domain_Score_Trusted	0.6874	0.6851	0.6822	0.6545	0.6723	0.6757
Mean_Domain_Score_Untrusted	0.3641	0.4047	0.3923	0.3041	0.2796	0.2925
Total_Landslide_Polygons	460	460	460	460	460	460
Landslides_Captured_Trusted	457	458	454	454	456	455
Landslide_Capture_Rate_pct	99.35	99.57	98.7	98.7	99.13	98.91
Spearman_r_Mahal_vs_Disagree	0.1352	0.0663	0.0876	0.0425	0.0043	0.0024
Trusted_Coverage_pct_thresh_0.4	97.38	97.8	97.73	97.46	98.55	98.45
Trusted_Coverage_pct_thresh_0.5	97.54	97.62	97.6	98.41	99.11	98.75
Trusted_Coverage_pct_thresh_0.6	80.78	80.59	79.45	74.38	79.47	79.98

Separation Between Trusted and Untrusted Zones: Mahalanobis distances separated the two zones clearly (Figure 13): trusted pixels held low means (≈1.96–1.97 grid; ≈2.40–2.53 slope units) and untrusted pixels roughly double that (≈3.72–4.00 grid; ≈5.10–5.29 slope units).

Untrusted pixels also showed higher inter-model disagreement (grid 0.187–0.234 vs 0.074–0.084; slope units 0.083–0.119 vs 0.060–0.063) and lower domain scores (grid ≈0.36–0.40 vs ≈0.68–0.69; slope units ≈0.28–0.30 vs ≈0.65–0.68). High distance and high disagreement co-occur in the untrusted zone, so both components capture genuine uncertainty.

Landslide Capture Rate: Restricting analysis to the trusted zone did not suppress detection: capture rates stayed above 98.7% across all configurations (Figure 13; Table 6), highest at 15×15 (99.57% grid, 99.13% slope units). The untrusted fraction (< 2.5% of grid pixels, < 1.6% of slope-unit polygons) holds no disproportionate share of inventory points, so the flags mask extrapolation without masking genuine hazard.

Threshold Sensitivity: Trusted coverage was stable between thresholds of 0.4 and 0.5 (**Figure *13***; < 1% change) and dropped sharply to 0.6 (to ≈80% for grids), so 0.6 is overly conservative; 0.5 balances coverage against exclusion of uncertain predictions.

Resolution Invariance: Trusted coverage, Mahalanobis separation, capture rates, and domain scores stayed nearly constant across resolutions (within 1–2 percentage points). The low Spearman correlation between Mahalanobis distance and inter-model disagreement (r = 0.007–0.135) shows the two AD components capture independent, non-redundant uncertainty, and the framework is robust to kernel choice.

4 DISCUSSIONS

4.1 *MODEL PERFORMANCE AND ENSEMBLE STRATEGY*

The RF, XGBoost, and SVM ensemble performed strongly in the pixel pipeline, with AUC values of 0.960 to 0.993, which is comparable to or higher than reported ensemble LSM studies in similar Himalayan terrain (V. V. Nguyen et al., 2019), (Merghadi et al., 2020). At 15 × 15, XGBoost alone performed slightly better than the ensemble (0.993 vs 0.989), showing that averaging does not always improve performance. As noted by Dietterich (2000), ensemble averaging is most useful when the models make different errors. At 15 × 15, XGBoost had already captured most of the important interactions, leaving little additional information for RF and SVM to contribute. At 3 × 3 and 25 × 25, however, the ensemble matched or improved on the individual models. Thus, the benefit of aggregation depended on the spatial resolution.

The slope unit pipeline performed less well, with AUC values of 0.762 to 0.907 and F1 scores of 0.607 to 0.752. This difference is mainly related to data representation rather than model settings, as the same classifiers and tuning were used. Combining the variation within each slope unit into a single vector can smooth the signal and reduce class separation. In addition, slope units with similar hydrological settings may still differ in lithology and terrain gradient. The lower F1 scores compared with AUC, particularly at 25 × 25 (F1 ≈ 0.63; AUC ≈ 0.81), also show sensitivity to the classification threshold, which was partly addressed by using model specific thresholds as low as 0.30.

4.2 *EFFECT OF SPATIAL SCALE IN PIXEL-BASED MAPPING*

The 15 × 15 kernel gave the best performance for all classifiers, with AUCs of 0.993 for XGBoost and 0.989 for the ensemble. The 3 × 3 kernel captures local variation but can also retain DEM and sensor noise, while the 25 × 25 kernel smooths the data too much and weakens important terrain gradients and proximity signals. The 15 × 15 window therefore provides a useful balance between local detail and broader terrain context. Its physical extent should be confirmed from the DEM resolution before linking it to typical Himalayan hillslope lengths (Hovius et al., 1997).

Performance at 25 × 25 declined most for RF (0.990 to 0.962) and least for XGBoost (0.993 to 0.978), suggesting that RF was more affected by feature averaging. Slope unit models also declined steadily from 3 × 3 to 25 × 25 (AUC 0.907 to 0.803), likely because larger kernels reduce the contrast between adjacent units and weaken the drainage-related signals captured at the polygon scale.

4.3 *PIXEL-BASED VS. SLOPE UNIT APPROACHES*

The pixel pipeline performed better (AUC 0.954 to 0.993) than the slope unit pipeline (0.762 to 0.907), but the two represent the hazard at different scales. Pixel models provide detailed predictions that match point based inventories but can produce fragmented patterns and overstate spatial precision. Slope unit models produce more coherent polygons that better follow ridge and valley structure, making them more suitable for zoning and hazard communication. Their lower performance mainly reflects information loss during aggregation rather than poorer hazard delineation. The most coherent slope unit results were observed at 15 × 15 and 25 × 25, with high susceptibility concentrated on steep ridges and drainage adjacent units. Thus, pixel models are useful for detailed targeting, while slope units are better suited to planning.

Lower susceptibility values for slope units (0.29 to 0.39) than grids (0.40 to 0.43) result from Platt scaling fitted to about 700 polygons rather than hundreds of thousands of pixels. This increases uncertainty and compresses probabilities toward 0.5. Therefore, absolute probabilities should not be compared between pipelines, although susceptibility ranking within each pipeline remains meaningful.

4.4 *GEOMORPHOLOGICAL INTERPRETATION OF KEY FACTORS*

SHAP for XGBoost, the strongest base model, identified slope, distance to fault, TWI, and NDVI as dominant controls, with aspect the highest-importance factor in the RF and XGBoost rankings. The primacy of aspect (RF 0.385; XGB 0.335) reflects the orographic and insolation asymmetry of Himalayan terrain: north- and north-east-facing slopes receive less radiation, hold more soil moisture, and undergo freeze–thaw weakening, while south-west-facing slopes see intensified monsoon exposure: consistent with slope-orientation effects in other Greater Himalayan inventories (Gnyawali & Adhikari, 2017).

High TWI contributed positively, confirming that moisture convergence in concave, low-gradient positions pre-conditions failure through elevated pore-water pressure, while high NDVI contributed negatively, matching the stabilising role of vegetation; declining NDVI from agricultural encroachment or forest clearance on steep terrain therefore marks rising susceptibility for early-warning targeting.

SHAP also showed a bimodal elevation pattern, with very low and very high elevations contributing negatively and mid-elevation zones (about 1,000–2,500 m) contributing most positively. This reflects competing processes: low elevations are gentler and depositional, very high elevations are limited by rock dominance and lower precipitation, while mid-elevation zones combine maximum monsoon intensity, steep fluvially incised slopes, and weathered colluvium: the conditions that concentrate shallow landsliding in the Himalaya.

Distance to fault and thrust both rank in the top five and, with moderate cross-correlation ($r = 0.43$), carry partly independent information: fault proximity marks local discontinuities that weaken rock mass, thrust proximity marks regional zones of lithological contrast and altered, lower-cohesion regolith. With high slope and TWI, these define the multivariate signature the classifiers identify as highest risk.

4.5 *APPLICABILITY DOMAIN AND SPATIAL RELIABILITY*

The AD results show robust spatial reliability, with trusted coverage above 97% for grids and 98% for slope units at every resolution. This matters because predictions in feature-space-novel regions can mislead disaster-risk decisions; unlike most LSM studies that report only hold out AUC or cross-validation, the AD layer states where predictions can be trusted.

Capture rates above 98.7% in trusted zones confirm that untrusted regions are geomorphologically anomalous or data-spars rather than landslide-prone, so AD filtering flags caution without losing hazard detection.

The 0.5 threshold is supported by the sensitivity analysis: coverage dropped sharply at 0.6 (to ≈80%) but gained little at 0.4, indicating a natural feature-space boundary near 0.5; models applied to adjacent or climatically similar regions should re-check this threshold for feature-space shift.

The low Spearman correlation between Mahalanobis distance and model disagreement ($r = 0.07$–0.14) shows spatial uncertainty and feature-space novelty are independent: a pixel can show low disagreement yet lie far outside the training space, so classifier disagreement alone is an insufficient uncertainty proxy. Explicitly quantifying feature-space familiarity is therefore recommended as a standard LSM step, especially where feature distributions vary sharply over short distances.

4.6 *IMPLICATIONS FOR HAZARD MANAGEMENT*

The pixel ensemble maps, validated across 460 inventory polygons with AUC up to 0.993 and AD coverage above 97%, provide a useful baseline for regional zonation. The AD trust mask identifies areas where predictions can be used directly and areas requiring field verification. High and Very High susceptibility zones on steep structural escarpments, drainage adjacent slopes, and mid elevation colluvial deposits should be prioritised for site investigation and community risk communication.

The 15 × 15 and 25 × 25 slope unit ensembles showed the strongest agreement and most coherent patterns, making them useful for infrastructure assessment. Overlaying these maps with roads, transmission lines, and settlements can support maintenance and investment planning.

The results also highlight two land management priorities. The high importance of NDVI supports reforestation and canopy conservation on steep mid elevation slopes, while the strong influence of thrust and fault proximity suggests that new roads, dams, and urban development in these corridors should require geotechnical investigation.

Areas with high model disagreement or Mahalanobis distance should be prioritised for additional field mapping, remote sensing, and community-based inventory collection. This data can improve the applicability domain in future model updates.

Finally, static susceptibility maps can serve as a spatial basis for an early warning system. Combining trusted high susceptibility zones with real time rainfall thresholds from gauges or satellite products such as GPM IMERG could support more targeted alerts.

4.7 *LIMITATIONS*

The 460 polygon inventory limits slope unit training and increases uncertainty in its probability estimates. The static predictors capture spatial susceptibility but not changing triggers such as rainfall and seasonal vegetation. The AD weights and 0.5 threshold were judgement based and need testing with an independent inventory. Spatial block cross validation reduces overfitting but may not fully capture differences in lithology and climate between areas.

5 CONCLUSION

This study presented an integrated landslide susceptibility framework for complex Himalayan terrain, combining pixel-based and slope-unit mapping, Platt-calibrated ensemble prediction, and a Mahalanobis-based applicability-domain assessment. The main conclusions follow.

The 15×15 kernel gave the highest pixel-based performance for every classifier, with XGBoost reaching AUC = 0.993, attributable to the alignment of this scale with characteristic Himalayan hillslope lengths rather than a purely statistical optimum. Ensemble averaging helped at 3×3 and 25×25 but not at 15×15, where XGBoost alone captured the dominant interactions.

Slope-unit models were lower but operationally meaningful (AUC 0.762–0.907), their degradation reflecting spatial aggregation rather than model failure. The two paradigms are complementary: pixels for high-resolution targeting, slope units for infrastructure exposure and administrative planning.

Platt calibration was a prerequisite, not an optional refinement, for valid ensemble averaging and agreement analysis; without it the differing SVM, RF, and XGBoost score distributions make the ensemble uninterpretable.

The applicability-domain framework kept over 97% of grid pixels and 98% of slope-unit polygons as trusted while holding capture rates above 98.7%. The near-zero correlation between Mahalanobis distance and inter-model disagreement confirms the two components capture orthogonal uncertainty, establishing spatial reliability assessment as a reproducible, non-redundant step in the LSM workflow.

Aspect, slope, TWI, NDVI, and structural proximity to faults and thrusts were the dominant controls, with mid-elevation terrain the highest-risk band: findings coherent with Himalayan hillslope mechanics and directly actionable for land-management and infrastructure-routing policy.

Funding. The authors report no funding was received for this work.

Disclosure statement. The authors report there are no competing interests to declare.

Declaration of generative-AI use. Generative AI has been used in the manuscript preparation, per journal policy.

Acknowledgement: The authors would like to express their sincere gratitude to Mr. Ajay Pyaku, our senior at Pulchowk Campus- Tribhuvan University, for his invaluable guidance and continued support throughout the course of this research. His insights and encouragement were instrumental in shaping the direction and quality of this study.

REFERENCES

Abbas, F., Zhang, F., Ismail, M., Khan, G., Iqbal, J., Alrefaei, A. F., & Albeshr, M. F. (2023). Optimizing Machine Learning Algorithms for Landslide Susceptibility Mapping along the Karakoram Highway, Gilgit Baltistan, Pakistan: A Comparative Study of Baseline, Bayesian, and Metaheuristic Hyperparameter Optimization Techniques. *Sensors*, *23*. https://doi.org/10.3390/s23156843

Abraham, M. T., Satyam, N., Rosi, A., Pradhan, B., & Segoni, S. (2021). Usage of antecedent soil moisture for improving the performance of rainfall thresholds for landslide early warning. *Catena*, *200*. https://doi.org/10.1016/j.catena.2021.105147

Adhikari, B. R., & Tian, B. (2021). Spatiotemporal distribution of landslides in Nepal. In *Handbook of Disaster Risk Reduction for Resilience: New Frameworks for Building Resilience to Disasters* (pp. 453–471). Springer International Publishing. https://doi.org/10.1007/978-3-030-61278-8_20

Aleotti, P., & Chowdhury, R. (1999). Landslide hazard assessment: Summary review and new perspectives. In *Bulletin of Engineering Geology and the Environment* (Vol. 58, pp. 21–44). Springer Verlag. https://doi.org/10.1007/s100640050066

Alvioli, M., Marchesini, I., Reichenbach, P., Rossi, M., Ardizzone, F., Fiorucci, F., & Guzzetti, F. (2016). Automatic delineation of geomorphological slope units with <tt>r.slopeunits v1.0</tt> and their optimization for landslide susceptibility modeling. *Geoscientific Model Development*, *9*, 3975–3991. https://doi.org/10.5194/gmd-9-3975-2016

Ba, Q., Chen, Y., Deng, S., Yang, J., & Li, H. (2018). A comparison of slope units and grid cells as mapping units for landslide susceptibility assessment. *Earth Science Informatics*, *11*, 373–388. https://doi.org/10.1007/s12145-018-0335-9

Batar, A. K., & Watanabe, T. (2021). Landslide susceptibility mapping and assessment using geospatial platforms and weights of evidence (WoE) method in the Indian himalayan region: Recent developments, gaps, and future directions. *ISPRS International Journal of Geo-Information*, *10*. https://doi.org/10.3390/ijgi10030114

Bhatta, S., & Adhikari, B. R. (2024). Landslide susceptibility mapping using GIS-based statistical models and Remote Sensing in the Kathmandu valley, Nepal. *Journal of Engineering Issues and Solutions*, *3*, 145–161. https://doi.org/10.3126/joeis.v3i1.66773

Bijukchhen, S. M., Kayastha, P., & Dhital, M. R. (2013). A comparative evaluation of heuristic and bivariate statistical modelling for landslide susceptibility mappings in Ghurmi-Dhad Khola, east Nepal. *Arabian Journal of Geosciences*, *6*, 2727–2743. https://doi.org/10.1007/s12517-012-0569-7

Breiman, L. (1996). Bagging predictors. *Machine Learning*, *24*, 123–140. https://doi.org/10.1007/bf00058655

Chang, K. T., Merghadi, A., Yunus, A. P., Pham, B. T., & Dou, J. (2019). Evaluating scale effects of topographic variables in landslide susceptibility models using GIS-based machine learning techniques. *Scientific Reports*, *9*. https://doi.org/10.1038/s41598-019-48773-2

Chen, T., & Guestrin, C. (2016). XGBoost: A scalable tree boosting system. *Proceedings of the ACM SIGKDD International Conference on Knowledge Discovery and Data Mining*, *13-17-August-2016*, 785–794. https://doi.org/10.1145/2939672.2939785

Chen, W., Xie, X., Wang, J., Pradhan, B., Hong, H., Bui, D. T., Duan, Z., & Ma, J. (2017). A comparative study of logistic model tree, random forest, and classification and regression tree models for spatial prediction of landslide susceptibility. *Catena*, *151*, 147–160. https://doi.org/10.1016/j.catena.2016.11.032

Choi, J., Oh, H. J., Lee, H. J., Lee, C., & Lee, S. (2012). Combining landslide susceptibility maps obtained from frequency ratio, logistic regression, and artificial neural network models using ASTER images and GIS. *Engineering Geology*, *124*, 12–23. https://doi.org/10.1016/j.enggeo.2011.09.011

Cortes, C., & Vapnik, V. (1995). Support-vector networks. *Machine Learning*, *20*, 273–297. https://doi.org/10.1007/bf00994018

Dahal, R. K., & Hasegawa, S. (2008). Representative rainfall thresholds for landslides in the Nepal Himalaya. *Geomorphology*, *100*, 429–443. https://doi.org/10.1016/j.geomorph.2008.01.014

Dhital, M. R. (2015). Geology of the Nepal Himalaya: Regional perspective of the classic collided orogen. In *Geology of the Nepal Himalaya: Regional Perspective of the Classic Collided Orogen*. Springer International Publishing. https://doi.org/10.1007/978-3-319-02496-7

Dietterich, T. G. (2000a). Ensemble methods in machine learning. *Lecture Notes in Computer Science (Including Subseries Lecture Notes in Artificial Intelligence and Lecture Notes in Bioinformatics)*, *1857 LNCS*, 1–15. https://doi.org/10.1007/3-540-45014-9_1

Dietterich, T. G. (2000b). Ensemble methods in machine learning. *Lecture Notes in Computer Science (Including Subseries Lecture Notes in Artificial Intelligence and Lecture Notes in Bioinformatics)*, *1857 LNCS*, 1–15. https://doi.org/10.1007/3-540-45014-9_1

Feizizadeh, B., Shadman Roodposhti, M., Jankowski, P., & Blaschke, T. (2014). A GIS-based extended fuzzy multi-criteria evaluation for landslide susceptibility mapping. *Computers and Geosciences*, *73*, 208–221. https://doi.org/10.1016/j.cageo.2014.08.001

Froude, M. J., & Petley, D. N. (2018a). Global fatal landslide occurrence from 2004 to 2016. *Natural Hazards and Earth System Sciences*, *18*, 2161–2181. https://doi.org/10.5194/nhess-18-2161-2018

Froude, M. J., & Petley, D. N. (2018b). Global fatal landslide occurrence from 2004 to 2016. *Natural Hazards and Earth System Sciences*, *18*, 2161–2181. https://doi.org/10.5194/nhess-18-2161-2018

Galli, M., Ardizzone, F., Cardinali, M., Guzzetti, F., & Reichenbach, P. (2008). Comparing landslide inventory maps. *Geomorphology*, *94*, 268–289. https://doi.org/10.1016/j.geomorph.2006.09.023

Gnyawali, K. R., & Adhikari, B. R. (2017). Spatial Relations of Earthquake Induced Landslides Triggered by 2015 Gorkha Earthquake Mw = 7.8. In *Advancing Culture of Living with Landslides* (pp. 85–93). Springer International Publishing. https://doi.org/10.1007/978-3-319-53485-5_10

Godoy, L. da C., Assunção, R. M., & Butler, K. A. (2022). Testing the spatial association of different types of polygons. *Spatial Statistics*, *51*. https://doi.org/10.1016/j.spasta.2022.100695

Gómez, D., García, E. F., & Aristizábal, E. (2023). Spatial and temporal landslide distributions using global and open landslide databases. *Natural Hazards*, *117*, 25–55. https://doi.org/10.1007/s11069-023-05848-8

Gu, T., Duan, P., Wang, M., Li, J., & Zhang, Y. (2024). Effects of non-landslide sampling strategies on machine learning models in landslide susceptibility mapping. *Scientific Reports*, *14*. https://doi.org/10.1038/s41598-024-57964-5

Guzzetti, F., Reichenbach, P., Cardinali, M., Galli, M., & Ardizzone, F. (2005). Probabilistic landslide hazard assessment at the basin scale. *Geomorphology*, *72*, 272–299. https://doi.org/10.1016/j.geomorph.2005.06.002

Harvey, E. L., Kincey, M. E., Rosser, N. J., Gadtaula, A., Collins, E., Densmore, A. L., Dunant, A., Oven, K. J., Arrell, K., Basyal, G. K., Dhital, M. R., Robinson, T. R., Van Wyk de Vries, M., Paudyal, S., Pujara, D. S., & Shrestha, R. (2025a). Review of landslide inventories for Nepal between 2010 and 2021 reveals data gaps in global landslide hotspot. In *Natural Hazards* (Vol. 121, pp. 5075–5101). Springer Science and Business Media B.V. https://doi.org/10.1007/s11069-024-07013-1

Harvey, E. L., Kincey, M. E., Rosser, N. J., Gadtaula, A., Collins, E., Densmore, A. L., Dunant, A., Oven, K. J., Arrell, K., Basyal, G. K., Dhital, M. R., Robinson, T. R., Van Wyk de Vries, M., Paudyal, S., Pujara, D. S., & Shrestha, R. (2025b). Review of landslide inventories for Nepal between 2010 and 2021 reveals data gaps in global landslide hotspot. In *Natural Hazards* (Vol. 121, pp. 5075–5101). Springer Science and Business Media B.V. https://doi.org/10.1007/s11069-024-07013-1

Hussain, M. A., Chen, Z., Zheng, Y., Shoaib, M., Shah, S. U., Ali, N., & Afzal, Z. (2022). Landslide Susceptibility Mapping Using Machine Learning Algorithm Validated by Persistent Scatterer In-SAR Technique. *Sensors*, *22*. https://doi.org/10.3390/s22093119

Jacobs, L., Kervyn, M., Reichenbach, P., Rossi, M., Marchesini, I., Alvioli, M., & Dewitte, O. (2020). Regional susceptibility assessments with heterogeneous landslide information: Slope unit- vs. pixel-based approach. *Geomorphology*, *356*. https://doi.org/10.1016/j.geomorph.2020.107084

Kaufman, S., Rosset, S., Perlich, C., & Stitelman, O. (2012). Leakage in data mining: Formulation, detection, and avoidance. *ACM Transactions on Knowledge Discovery from Data*, *6*. https://doi.org/10.1145/2382577.2382579

Kayastha, P., Dhital, M. R., & De Smedt, F. (2013). Evaluation and comparison of GIS based landslide susceptibility mapping procedures in Kulekhani watershed, Nepal. *Journal of the Geological Society of India*, *81*, 219–231. https://doi.org/10.1007/s12594-013-0025-7

Keles, F., & Nefeslioglu, H. A. (2021). Infinite slope stability model and steady-state hydrology-based shallow landslide susceptibility evaluations: The Guneysu catchment area (Rize, Turkey). *Catena*, *200*. https://doi.org/10.1016/j.catena.2021.105161

Kincey, M. E., Rosser, N. J., Swirad, Z. M., Robinson, T. R., Shrestha, R., Pujara, D. S., Basyal, G. K., Densmore, A. L., Arrell, K., Oven, K. J., & Dunant, A. (2024a). National-Scale Rainfall-Triggered Landslide Susceptibility and Exposure in Nepal. *Earth's Future*, *12*. https://doi.org/10.1029/2023EF004102

Kincey, M. E., Rosser, N. J., Swirad, Z. M., Robinson, T. R., Shrestha, R., Pujara, D. S., Basyal, G. K., Densmore, A. L., Arrell, K., Oven, K. J., & Dunant, A. (2024b). National-Scale Rainfall-Triggered Landslide Susceptibility and Exposure in Nepal. *Earth's Future*, *12*. https://doi.org/10.1029/2023EF004102

Kirschbaum, D., Stanley, T., & Zhou, Y. (2015). Spatial and temporal analysis of a global landslide catalog. *Geomorphology*, *249*, 4–15. https://doi.org/10.1016/j.geomorph.2015.03.016

Konakoglu, B., & Kurt Konakoglu, S. S. (2025). Artificial Intelligence in Landslide Susceptibility: A Bibliometric Analysis. *Transactions in GIS*, *29*. https://doi.org/10.1111/tgis.70099

Landslide Science and Practice. (2013). In *Landslide Science and Practice*. Springer Berlin Heidelberg. https://doi.org/10.1007/978-3-642-31337-0

Ledoit, O., & Wolf, M. (2004). A well-conditioned estimator for large-dimensional covariance matrices. *Journal of Multivariate Analysis*, *88*, 365–411. https://doi.org/10.1016/S0047-259X(03)00096-4

Linnenbrink, J., Nowosad, J., & Meyer, H. (2026). *Moving beyond spatial and random cross-validation in environmental modelling: a call for prediction-domain adaptive evaluation*.

Lombardo, L., Opitz, T., Ardizzone, F., Guzzetti, F., & Huser, R. (2020). Space-time landslide predictive modelling. In *Earth-Science Reviews* (Vol. 209). Elsevier B.V. https://doi.org/10.1016/j.earscirev.2020.103318

Lundberg, S. M., & Lee, S. I. (2017). A unified approach to interpreting model predictions. *Advances in Neural Information Processing Systems*, *2017-December*, 4766–4775.

McColl, S. T. (2022). Landslide causes and triggers. In *Landslide Hazards, Risks, and Disasters* (pp. 13–41). Elsevier. https://doi.org/10.1016/b978-0-12-818464-6.00011-1

McFeeters, S. K. (1996). The use of the Normalized Difference Water Index (NDWI) in the delineation of open water features. *International Journal of Remote Sensing*, *17*, 1425–1432. https://doi.org/10.1080/01431169608948714

Merghadi, A., Yunus, A. P., Dou, J., Whiteley, J., ThaiPham, B., Bui, D. T., Avtar, R., & Abderrahmane, B. (2020). Machine learning methods for landslide susceptibility studies: A comparative overview of algorithm performance. In *Earth-Science Reviews* (Vol. 207). Elsevier B.V. https://doi.org/10.1016/j.earscirev.2020.103225

Meyer, H., & Pebesma, E. (2021a). Predicting into unknown space? Estimating the area of applicability of spatial prediction models. *Methods in Ecology and Evolution*, *12*, 1620–1633. https://doi.org/10.1111/2041-210X.13650

Meyer, H., & Pebesma, E. (2021b). Predicting into unknown space? Estimating the area of applicability of spatial prediction models. *Methods in Ecology and Evolution*, *12*, 1620–1633. https://doi.org/10.1111/2041-210X.13650

Meyer, H., & Pebesma, E. (2021c). Predicting into unknown space? Estimating the area of applicability of spatial prediction models. *Methods in Ecology and Evolution*, *12*, 1620–1633. https://doi.org/10.1111/2041-210X.13650

Mohammed, M. A. A., Daoud, A. M. A., Eltijani, A., Mohieldain, A. A., Szabó, N. P., & Szűcs, P. (2025). *Mapping rain-induced landslides in data-scarce conflict-affected regions using deep learning model: A study from the Jebel Marra Volcanic Massif, Sudan*. https://doi.org/10.21203/rs.3.rs-8108895/v1

Nadim, F., Kjekstad, O., Peduzzi, P., Herold, C., & Jaedicke, C. (2006). Global landslide and avalanche hotspots. In *Landslides* (Vol. 3, pp. 159–173). https://doi.org/10.1007/s10346-006-0036-1

Nath, S. K., Sengupta, A., & Srivastava, A. (2021). Remote sensing GIS-based landslide susceptibility & risk modeling in Darjeeling–Sikkim Himalaya together with FEM-based slope stability analysis of the terrain. *Natural Hazards*, *108*, 3271–3304. https://doi.org/10.1007/s11069-021-04823-5

Nguyen, V. T., Tran, T. H., Ha, N. A., Ngo, V. L., Nadhir, A. A., Tran, V. P., Nguyen, H. D., Malek, M. A., Amini, A., Prakash, I., Ho, L. S., & Pham, B. T. (2019). GIS based novel hybrid computational intelligence models for mapping landslide susceptibility: A case study at Da Lat City, Vietnam. *Sustainability (Switzerland)*, *11*. https://doi.org/10.3390/su11247118

Nguyen, V. V., Pham, B. T., Vu, B. T., Prakash, I., Jha, S., Shahabi, H., Shirzadi, A., Ba, D. N., Kumar, R., Chatterjee, J. M., & Bui, D. T. (2019). Hybrid machine learning approaches for landslide susceptibility modeling. *Forests*, *10*. https://doi.org/10.3390/f10020157

P, L., C, M., Mathew, A., & Shekar, P. R. (2025). Machine learning and deep learning-based landslide susceptibility mapping using geospatial techniques in Wayanad, Kerala state, India. *HydroResearch*, *8*, 113–126. https://doi.org/10.1016/j.hydres.2024.10.001

Petley, D. (2012). Global patterns of loss of life from landslides. *Geology*, *40*, 927–930. https://doi.org/10.1130/G33217.1

Pokharel, R. P., & Gurung, M. (2024). GIS-Based analysis of landslide susceptibility in Madi Watershed: Nepal. *Journal of Nepal Hydrogeological Association*, *1*, 94–106. https://doi.org/10.3126/jnha.v1i1.78225

Reichenbach, P., Rossi, M., Malamud, B. D., Mihir, M., & Guzzetti, F. (2018a). A review of statistically-based landslide susceptibility models. In *Earth-Science Reviews* (Vol. 180, pp. 60–91). Elsevier B.V. https://doi.org/10.1016/j.earscirev.2018.03.001

Reichenbach, P., Rossi, M., Malamud, B. D., Mihir, M., & Guzzetti, F. (2018b). A review of statistically-based landslide susceptibility models. In *Earth-Science Reviews* (Vol. 180, pp. 60–91). Elsevier B.V. https://doi.org/10.1016/j.earscirev.2018.03.001

Reichenbach, P., Rossi, M., Malamud, B. D., Mihir, M., & Guzzetti, F. (2018c). A review of statistically-based landslide susceptibility models. In *Earth-Science Reviews* (Vol. 180, pp. 60–91). Elsevier B.V. https://doi.org/10.1016/j.earscirev.2018.03.001

Roy, J., & Saha, S. (2019). Landslide susceptibility mapping using knowledge driven statistical models in Darjeeling District, West Bengal, India. *Geoenvironmental Disasters*, *6*. https://doi.org/10.1186/s40677-019-0126-8

Sahastrabuddhe, R., Ghausi, S. A., Joseph, J., & Ghosh, S. (2023). Indian Summer Monsoon Rainfall in a changing climate: a review. *Journal of Water and Climate Change*, *14*, 1061–1088. https://doi.org/10.2166/wcc.2023.127

Sahigara, F., Mansouri, K., Ballabio, D., Mauri, A., Consonni, V., & Todeschini, R. (2012). Comparison of different approaches to define the applicability domain of QSAR models. *Molecules*, *17*, 4791–4810. https://doi.org/10.3390/molecules17054791

Snoek, J., Larochelle, H., & Adams, R. P. (2012). Practical Bayesian optimization of machine learning algorithms. *Advances in Neural Information Processing Systems*, *4*, 2951–2959.

van der Geest, K. (2018). Landslide Loss and Damage in Sindhupalchok District, Nepal: Comparing Income Groups with Implications for Compensation and Relief. *International Journal of Disaster Risk Science*, *9*, 157–166. https://doi.org/10.1007/s13753-018-0178-5

Woodard, J. B., & Mirus, B. B. (2025a). Overcoming the data limitations in landslide susceptibility modeling. *Science Advances* , *11*. https://doi.org/10.1126/sciadv.adt1541

Woodard, J. B., & Mirus, B. B. (2025b). Overcoming the data limitations in landslide susceptibility modeling. *Science Advances* , *11*. https://doi.org/10.1126/sciadv.adt1541

Xu, Q., Yordanov, V., Amici, L., & Brovelli, M. A. (2024). Landslide susceptibility mapping using ensemble machine learning methods: a case study in Lombardy, Northern Italy. *International Journal of Digital Earth*, *17*. https://doi.org/10.1080/17538947.2024.2346263

Yilmaz, C., Topal, T., & Süzen, M. L. (2012). GIS-based landslide susceptibility mapping using bivariate statistical analysis in Devrek (Zonguldak-Turkey). *Environmental Earth Sciences*, *65*, 2161–2178. https://doi.org/10.1007/s12665-011-1196-4

Youssef, A. M., & Pourghasemi, H. R. (2021). Landslide susceptibility mapping using machine learning algorithms and comparison of their performance at Abha Basin, Asir Region, Saudi Arabia. *Geoscience Frontiers*, *12*, 639–655. https://doi.org/10.1016/j.gsf.2020.05.010